FLUIDIC CONTROL OF AERODYNAMIC FORCES AND MOMENTS ON AN AXISYMMETRIC BODY

A Thesis
Presented to
The Academic Faculty

By

Philip S Abramson

In Partial Fulfillment
Of the Requirements for the Degree
Master of Science in Mechanical Engineering

Georgia Institute of Technology

December, 2009

FLUIDIC CONTROL OF AERODYNAMIC FORCES AND MOMENTS ON AN AXISYMMETRIC BODY

Approved by:

Dr. Ari Glezer
School of Mechanical Engineering
Georgia Institute of Technology

Dr. Bojan Vukasinovic
School of Mechanical Engineering
Georgia Institute of Technology

Dr. Mark Costello
School of Aerospace Engineering
Georgia Institute of Technology

Date Approved: November 16, 2009

ACKNOWLEDGMENTS

There are many people deserving thanks in the submission of the thesis. I would first like to thank my advisor, Dr. Ari Glezer, for his counsel, insight, and advice in this work. In addition, a debt of gratitude is owed to Dr. Bojan Vukasinovic for his continual leadership through the entire process. I would also like to thank the third member of my committee, Dr. Mark Costello. The support of The Army Research Office is gratefully acknowledged.

To everyone whom I worked with in the lab I would like to thank you for your help, support and entertainment. I would like to express my gratitude to research engineer John Culp for his help with the circuit design and coding. To my fellow lab mates through the years, Tom Boziak, Dan Brzozowski, Michael DeSalvo, Zach Douglas, Dave Garth, Abe Gissen, Donavan Gerty, Pablo Hidalgo, Hanif Hunter, Taylor Jones, John Kearney, Ashok Rejendar, Mark Simpson, Brett Warta, and George Woo, thanks to each of you for your friendship, advice, and being there to lend a hand.

Finally, I wish to give thanks to my family and particularly my parents for all their guidance, support, and being an enduring source of encouragement through the good and more challenging times through the years.

TABLE OF CONTENTS

LIST OF FIGURES

NOMENCLATURE

A_j	actuator orifice cross-sectional area
C_μ	jet momentum coefficient
C_L	lift coefficient
D	axisymmetric body diameter
R	axisymmetric body radius
k	turbulent kinetic energy
U	mean axial velocity component
V	mean radial velocity component
U_0	free stream velocity
U_j	average jet velocity
ρ	air density
T	jet period
Re_D	Reynolds number
Re_J	Jet Reynolds number
$\vec{F}_x$	momentum flux
$\vec{F}_\omega$	vorticity flux
St_D	Strouhal number
E	actuator voltage
E_s	strain gage readout
f	actuation frequency
f_M	modulation frequency

θ	temperature
t	time
ζ^*	mean vorticity component
F_D	drag force
F_L	lift force
F_S	side force
M_P	pitch moment
M_Y	yaw moment

SUMMARY

The aerodynamic steering forces and moments on a wind tunnel model of an axisymmetric bluff body are altered by induced segmented attachment of the separated flow over an azimuthal Coanda surface. The model is suspended in the wind tunnel by eight thin wires for minimal support interference within the wake. Each wire is instrumented with a miniature strain gage sensor for direct dynamic force measurements. Control is effected by an array of synthetic jet actuators that emanate from narrow, azimuthally-segmented slots, within a backward facing step. The aerodynamic effects are characterized using hot-wire anemometry and PIV measurements. In the first set of experiments, the array of synthetic jets is distributed around the perimeter of the circular tail end which is extended into a Coanda surface. The fluidic actuation results in segmented vectoring of the separated base flow along the rear Coanda surface and induces asymmetric aerodynamic forces and moments that can effect steering during flight. Transitory modulation of the actuation waveform of multiple actuators around the tail leads to the generation of significant dynamic side forces of controlled magnitude and direction with the potential utility for flight stabilization and fast maneuvering. In a second set of experiments the array of the synthetic jets is placed upstream of a mid-body axisymmetric cavity. A single jet induces a quasi-steady, nearly-matched force couple at the upstream and downstream ends of the cavity. Furthermore, transitory activation of multiple jets can be used to control the onset and sequencing of the couple forces and therefore the resultant force and moment.

CHAPTER 1

Introduction

Aerodynamic flow control research in recent years has demonstrated that forcing of a separated shear layer near solid surfaces can lead to local attachment and thereby to a significant alteration of the global flow and aerodynamic forces and moments. The present work exploits direct control of the separated shear layer around an axisymmetric body using aerodynamic flow control to generate both transient and sustained steering forces and moments.

The present work builds on the earlier work of Rinehart et. al. (2003) and McMichael et. al. (2004) on the use of flow control for the guidance of 40mm subsonic munitions. This was accomplished by controlling its steering aerodynamic forces and moments, paving the way for application of flow control to correct for cross winds and pointing errors. These authors applied projectile normal aerodynamic forces by exploiting transitory flow attachment on azimuthal segments of a rear Coanda surface (Rinehart et al., 2003). Actuation was provided by an integrated single synthetic jet driven by piezoelectric diaphragm and on-board electronic circuitry. The work demonstrated that the induced change in the aerodynamic force on the body was equivalent to the lift force at a 3° angle of attack. This effort also included the development of a flight control system and integration and validation of miniature sensors and flight control systems. The technology feasibility phase culminated with a 40-mm system demonstration (McMichael et al., 2004). The generated forces were sufficient to control the trajectory of the projectile in flight. Flight tests successfully demonstrated the utility of this flow control approach to achieve significant changes in the performance of spin stabilized guided munitions.

The present work also builds on the results of a numerical investigation of the controlled flow about an axisymmetric projectile by Sahu and Keavey (2001). The numerical work investigated the impact of location of synthetic jets on the axisymmetric body and the forces generated by their actuation. The actuation of synthetic jets placed in the nose region and tail of the projectile resulted in a 20% and 12% reduction in drag respectively. In addition, at a 4° angle of attack, the actuation of the tail jet increased the nose-up pitching moment by 30%. One of the conclusions of that work is that due to the unsteady nature of the flow, multiple jets around the body can provide control authority for maneuvering the projectile.

The goal of the present work is to build on the earlier findings of Rinehart et. al. (2003), and McMichael et. al. (2004), and investigate in detail the coupling between several flow control actuation mechanisms that lead to desired steering aerodynamic forces and moments. The time-dependent fluidic actuation and the resultant alteration of the base flow are intimately interconnected and not yet fully understood on a fundamental level.

The flow control approaches explore two different mechanisms. The first is control of the base flow of the projectile, by introducing localized attachment over a Coanda surface. The second is control within a mid-body cavity, where induced localized separation and vectoring are investigated. The resulting flow asymmetries provide platform-level aerodynamic control using both quasi-steady and transitory aerodynamic forces and moments for airborne steering. A key element of this flow control approach is the use of low-level actuation and aerodynamic amplification by the flow to achieve the desired control authority. Rigorous investigation and understanding of these mechanisms will advance the science of flow control and small-scale actuation, and allow an extension to larger projectiles.

The thesis is organized as follows: Chapter 2 provides a literature review on flow control associated with the project. Chapter 3 describes the experimental setup, and procedure. Chapters 4 and 5 discuss the results from control at the tail and mid-body cavity respectively. Finally, Chapter 6 summarizes the results in the conclusion section.

CHAPTER 2

Literature Review

2.1 Aerodynamic Flow Control

Active aerodynamic flow control techniques in recent years have primarily focused on mitigation of partial or complete flow separation over stalled aerodynamic surfaces (e.g., wing sections or flaps), where the separating shear layer is dominated by a strong coupling to the instability of the near wake and consequently by the nominally time-periodic formation and shedding of large-scale vortices (e.g., Wu et al., 1998). As a result, separation control strategies have mostly relied on the narrow-band receptivity of the separating flow to external actuation at Strouhal numbers that correspond to the unstable frequencies of the near wake.

Furthermore, active flow control of separated flows has been investigated in previous studies for the adjustment of lift and drag characteristics of aerodynamic bodies. This separation control manipulating the shear layer leads to a complete or partial reattachment of the separated flow. Some specific examples of flow control techniques used in previous studies have steady and unsteady blowing (Hsaio et. al., 1990), vibrating ribbons or flaps (Huang et. al., 1987), and usage of sound speakers (Collins and Zelenevitz, 1974).

Noted by Glezer et al. (2005), the actuation results in changes in the rate of entrainment which in the presence of the flow surface can lead to a Coanda-like deflection of the shed vortices towards the surface of the stalled airfoil and consequently to lift enhancement. In this approach which has been exploited with varying degrees of success since the early 1980s (e.g., Ahuja and Burrin, 1984, Neuberger and Wygnanski, 1987, and Seifert et al., 1993), the actuation period nominally scales with the advection time over the length of the separated flow domain (or the width of the wake) which for an airfoil implies a dimensionless actuation frequency St_{act} ~ O(1).

A different approach to flow control that is decoupled from the global flow (wake) instabilities emphasizes fluidic modification of the “apparent” aerodynamic shape of the surface by exploiting the interaction between arrays of surface-mounted fluidic actuators (e.g., synthetic jets) and the local cross flow (Smith and Glezer 1998, Amitay and Glezer 2002). The unique aspect about synthetic jets is that they do not require a fluid source and are formed locally from the fluid next to the surface from which they are embedded. They produce no net mass transfer to the system, although they inject momentum. The jets are formed by removing low momentum fluid near the wall and ejecting high momentum fluid into the flow as coherent vortical structures (Smith and Glezer, 1998). The interaction of the jets with the free stream flow over the surface leads to the formation of closed regions that displace local streamlines of the flow and this induces a change in shape of the surface and an apparent modification of the flow boundary (Glezer and Amitay, 2002). Synthetic jets have been modeled theoretically in the work of Gallas et. al. (2003), where a lumped element modeling code was used to predict their performance. The code predicted the peak output performance of the actuator based on the cavity and orifice geometry, and properties of the piezoelectric driver and showed good agreement with experiments.

Interactions between synthetic jets and the free stream can form trapped vorticity concentrations where the balance between the trapped and shed vorticity is continuously regulated by the actuators. When these interaction domains are formed upstream of flow separation, the alteration of the local pressure gradients can result in complete or partial bypass (or suppression) of separation (e.g., Amitay et. al. 1998, 2001, Amitay and Glezer 2002, and Glezer et. al. 2005). A key element of this approach is that control is attained at actuation frequencies that are nominally an order of magnitude higher than the characteristic flow frequency and are therefore can be decoupled from global flow instabilities. These investigations have also touched on the dynamics of the transitory attachment and separation processes that are accompanied by shedding of a train of successive vortices of opposite sense. Similar transient effects were also observed by Darabi and Wygnanski (2004) on an inclined flat surface.

Trapped vorticity flow control can also be effective when the baseline flow is fully attached, at low angles of attack (e.g., at cruise conditions). Chatlynne et al. (2001) and Amitay et al. (2001) showed that the formation of a stationary trapped vortex above an airfoil at low angles of attack leads to pressure drag reduction that is comparable to the magnitude of the pressure drag of the baseline configuration with minimal lift penalty. This approach was expanded by DeSalvo et al. (2002) and later by DeSalvo and Glezer (2006) to manipulate the Kutta condition of an airfoil using controlled concentrations of trapped vorticity near the trailing edge using a miniature O(0.01c) hybrid actuator similar to a Gurney flap. The changes in the flow near the trailing edge result in significant global aerodynamic effects over a broad range of angles of attack ($\alpha < 10^{o}$) that include a substantial reduction in pressure drag (and therefore an increase in L/D_{p}) and a significant increase in the pitching moment that can be continuously and bidirectionally adjusted by varying the strength of the actuation or the momentum coefficient.

In addition, aerodynamic flow control has also been applied to vector free stream flow or the separated shear layer around an object. Hammond and Redekopp (1997) applied suction on the rear of a bluff body to vector the flow and determined a relationship between the critical suction value and flow Reynolds number required to suppress vortex shedding in the wake. More recently, Lim and Redekopp (2002) used a numerical simulation to model suction ports on either side of an exiting jet. Results also indicated a critical suction value beyond which an asymmetric flapping motion was generated in the wake producing a lift to thrust ratio exceeding 15%. Smith and Glezer (2001) used a single synthetic jet to vector a steady conventional air jet. The steady jet is directed towards the synthetic jet due to the pressure difference and it reaches a vectoring angle of 20° for jet Reynolds Number of 4000. Smith and Glezer (1998) demonstrated that two synthetic jets run out of phase with each other will lead to vectoring of the net jet due to interaction of the adjacent vortex pairs. Furthermore, Allen and Smith (2009) used a synthetic jet to vector a primary steady flow jet over a Coanda surface. The work demonstrated that a momentum flux ratio of 0.28 between the synthetic jet and the primary jet was enough to initiate the vectoring.

2.2 Coanda Effect

The mitigation of flow separation near solid surfaces and thereby of global aerodynamic performance by exploiting the Coanda effect on surfaces has been addressed in a substantial body of work since the 1940s. The flow characteristics are typically modified by blowing a conventional jet along the surface. The attachment of the separated plane jet to an adjacent solid convex surface that extends to the edge of the nozzle is induced by the formation of a low-pressure region between the jet and the surface owing to entrainment (Newman, 1961). Depending on the surface angle relative to the jet centerline, the separated jet forms a recirculating flow bubble before it attaches to and flows along the surface. The Coanda effect has been the basis of circulation control over lifting surfaces in numerous aerodynamic systems. Wille and Fernholz, (1965) discussed the entrainment associated with a jet blowing over a Coanda surface and its general applications. In a recent review article, Englar (2000) notes that blowing over a Coanda surface with steady planar jets can yield ratios of lift augmentation to jet momentum flux as high as 80.

The Coanda effect has also been applied to control the wakes of bluff bodies for drag reduction. In an effort to improve the efficiency of motor vehicles, Englar (2001) used steady planar Coanda jets around the rear perimeter of commercial trucks and realized drag reduction of up to 10% (equivalent to 600% recovery on the applied thrust at $Re = 2.51 \cdot 10^6$). Similar work by Geropp and Odenthal (2000) on a two-dimensional bluff body ($Re = 9.9 \cdot 10^5$) also showed the ability of steady blowing on Coanda surfaces to increase base pressure by 50% and thereby reduce the drag by 10%.

Induced attachment for control of the aerodynamic drag on axisymmetric bodies has been investigated via *steady*, circumferentially-uniform blowing over Coanda surfaces. An example of this control was investigated by Freund and Mungal (1994) using steady, circumferentially-uniform blowing over Coanda surfaces at the aft corner of the body ($Re = 3.6 \cdot 10^5$) leading to drag reduction on the order of 15% at velocity ratios on the order of one. More recently, Corke et. al., (2008) analyzed the drag and lift generated with a tangential blowing plasma actuator placed upstream of a Coanda surface on an axisymmetric body. The effectiveness of the size of the Coanda radius was analyzed in terms of the angle of flow vectoring at $Re_D = 1.3\cdot10^5$. Upon actuation, the turning angle of the flow for all radii size reached 50°, the actuation produced the largest increase in turning angle of the flow for the smaller radius. In addition, upon actuation the drag on the body decreased by 30%.

Because the Coanda effect is associated with the attachment of an inherently separated flow to a solid surface, this flow configuration presents a unique opportunity to create asymmetric pressure distributions and net aerodynamic forces on various bluff bodies through differential, asymmetric activation. These effects were demonstrated by Rinehart et. al. (2003) on axisymmetric bluff bodies. Flow separation was effected around the periphery of the body just upstream of its aft end by a small rearward-facing step upstream of an azimuthal Coanda collar. The collar was positioned such that the base flow did not attach to the Coanda surface and time-periodic synthetic jet actuation was used to effect attachment on command. This investigation explored the effects of Coanda radius and jet strength on the level of the reaction force normal to the free stream (lift), and examined transient flow response to momentary activation of the synthetic jet. In a related investigation, McMichael et al. (2004) exploited this flow control approach to the separated base flow of an axisymmetric 40 mm spin stabilized projectile to effect aerodynamic steering forces and moments that were sufficient to control the trajectory of the projectile in flight.

2.3 Other Control Approaches on Axisymmetric Bodies

Flow control around axisymmetric bodies specifically has been investigated in order to explore drag reduction. Parsons et. al. (1974) used mathematical modeling to determine an optimal shape of an axisymmetric body for minimal drag. A polynomial was used to define a round nose, tail boom shape, and laminar flow was maintained as long as possible to minimize the drag. Koenig and Roshko (1984) placed a disk ahead of a cylinder to control the separating shear layer and reattachment. The cylinder was rigidly mounted, and a sting mount was connected to the disk. The sting mount was connected to a force balance, used to determine how the drag on the cylinder varied with the size and position of the front disk. Weickgenannt and Monkewitz (2000) investigated the utility of aft mounted control discs extended short distances behind blunt bases. They observed four vortex-shedding regimes; no effect near the base, followed by a sharp increase in shedding and drag, leading to an interval of reduced shedding and drag (~20%), concluding with the bodies displaying independent, additive effects. The mechanism of drag reduction was observed to be the "choking" of reverse flow from the wake to the gap cavity, which reduced the cavity pressure and turned the body shedding layer inward, tightening the wake and reducing drag. Kornilov (2005) attached mini fins along the length of an axisymmetric body to modify the boundary layer, and this reduced the skin friction drag which produced an overall drag reduction of 15%. Sigurdson (1995) studied the separation bubble forming around a streamwise-oriented cylinder downstream of a sharp-edged blunt face. Control was applied at the point of separation in order to decrease drag through reducing the reattachment length. It was observed that drag reduction increased linearly with forcing amplitude, reaching a maximum of 15% reduction. Using a more novel approach, Higuchi et. al. (2006) levitated a blunt faced cylinder using a magnetic field in a wind tunnel to measure drag without any interference. The work demonstrated that minimum drag occurs when separated flow reattaches close to the rear of the cylinder.

Furthermore, flows around cavities on axisymmetric bodies have been investigated in numerous investigations, predominantly motivated by their application to the drag reduction and their effects on flow stability. In particular, a significant interest in flow over such cavities is related to the resonance of the flow, which can produce self sustaining oscillations and large scale vortical structures, which can produce noise, structural vibrations, and undesirable moments (Cattafesta III et. al. 2003).

Gharib and Roshko (1987) investigated the effects of cavity flow oscillation on the overall drag on an axisymmetric body. It was found that there was a critical value of cavity width to depth ratio which results in a drag increase to $C_D = 0.4$. However, they observed that small cavity widths produce minimal drag which is smaller than the friction drag that would be associated with a solid surface in the absence of a cavity. In a related work, Howard and Goodman (1985) used a series of shallow cavities to investigate drag reduction on an axisymmetric bluff body. They determined that the degree of drag reduction provided by the cavities was a function of their location and the flow Reynolds number. With cavities placed in series towards the back of the body and a Re_D greater than 10^5, a 35% drag reduction was evident. Furthermore, Powers (1991) investigated drag reduction on a cylindrical body of revolution in flows ranging from Mach 0.3 to 0.93. The work demonstrated that the presence of a cavity can cause a slight reduction on the base drag, with the reduction increasing monotonically with increasing Mach Number. Drag reduction of $\Delta C_D = 0.05$ and 0.08 were shown for Mach number 0.3 and 0.93 respectively.

A number of investigations have focused on the reduction of flow resonance in axisymmetric cavities for the purpose of reducing vibrations, noise, and undesirable moments. For example, flow over an open bomb-bay hatch can lead potentially damaging structural vibrations to an aircraft. Undesirable pitching moments can arise when the flow over the cavity turns inward and follows the contour of the cavity (Ritchie et. al. 2005). Internal Rossiter Oscillation modes occur when the subsonic flow separates over the length of the cavity. These natural frequencies and vibration modes are caused by feedback of the separated shear layer at the downstream end of the cavity (Rossiter, 1964). A model that described the vorticity distribution in the separating mixing layer along with discrete frequencies that are associated with the cavity geometry was developed by Colonius (2001). Gharib and Roshko (1987) observed that the length of the axisymmetric cavity was the driving factor for the formation of the Rossiter modes, and oscillations start when $b/\theta > 80$ where b is the cavity width and θ is the shear layer momentum thickness.

There have been a number of attempts to reduce the cavity resonance modes. Sarohia and Massier (1974), injected mass directly into the base of an axisymmetric cavity and reported that all the modes were suppressed although a large mass injection rate of 15% (injection mass to mass flow rate through cavity) was required. Mendoza and Ahuja (1996) used a jet blowing at the upstream edge of a cavity to thicken the boundary layer. The jet was guided using a Coanda surface, such the jet faced upstream upon ejection into the flow. This thickening reduced the feedback through the cavity and reduced the flow tones on the order of 30 dB.

CHAPTER 3

Experimental Setup and Procedures

The present experiments focus on fluidic manipulation of the aerodynamic forces and moments on a body of revolution which is shown schematically in Figures 3.1 and 3.2. Measurements of the induced aerodynamic forces and measurements of the flow in the near wake are conducted in an open-return wind tunnel at Georgia Tech having a test section measuring 91cm on the side with a speed up to 40 m/s. The fluidic control forces and moments are generated using an azimuthal array of four synthetic jet actuators that are equally distributed along the perimeter of either the tail or upstream of a mid-body cavity. Jet actuation leads to the partial attachment of a segment of the separated shear layer resulting in a reaction force by the turning of the outer flow into the wake region at the tail or the mid-body cavity. In the first set of experiments, the fluidic control is applied at the tail of the body, and in the second set, the control is applied at the upstream edge of a mid-body cavity in the axisymmetric body.

3.1 Wind Tunnel Model

The axisymmetric model is constructed using stereo-lithographed and aluminum components. The model with control at the tail is 80mm in diameter and 150mm long, as shown in Figure 3.1. The nose and tail are coupled together using a central shaft. The tail assembly contains four independently-driven, piezoelectric actuators that generate synthetic jets. The rear component has a Coanda surface of constant radius of 12mm with cut-in grooves along the orifice edges that guide the jet flow and prevent azimuthal spreading. The adjoining backward-facing step to the circumference of the body is 1.5 mm in height. The step is utilized to force the separation line to be axisymmetric, and its height is shallow enough to enable local flow attachment when the control jet is activated, but high enough to prevent attachment of the free stream flow in the absence of the jet.

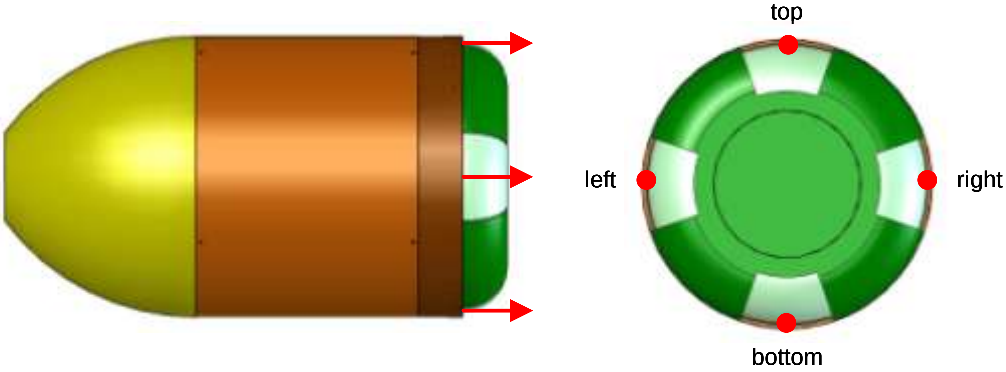

Figure 3.1. *Side- and upstream-views of the wind tunnel model, control at wake. Arrows mark the jet centerlines.*

In the second model, where control was applied at the upstream edge of a mid-body cavity, the jet actuation leads to the vectoring of the outer flow into the cavity. It also is comprised of modular aluminum and sterolithography components measuring 80mm in diameter and 220mm in length, shown in Figure 3.2. Adjacent to the nose, there is the mid-body cavity section which measures 40 mm in length, 32 mm in depth and is 84 mm behind the nose. The upstream end of this cavity houses four independently-driven, piezoelectric actuators that generate synthetic jets. Similar to the previous model, there is an adjoining backward facing step to the circumference of the body 1.5 mm in height at the location of the orifice, followed by a constant radius Coanda surface of 25mm.

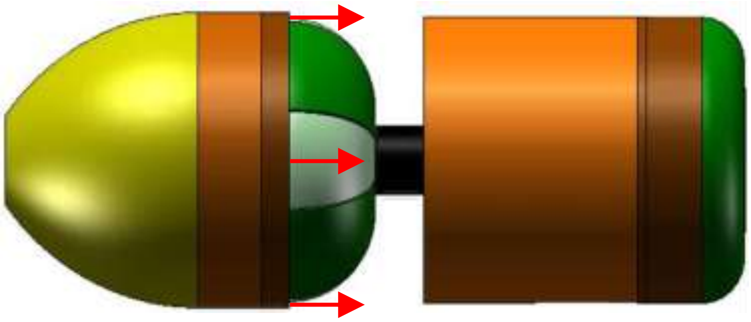

Figure 3.2. *Side view of the axisymmetric wind tunnel model, control upstream of cavity. Arrows mark the jet centerlines.*

The backward facing step upstream of the Coanda surface, in both models, is utilized to form the axisymmetric separation boundary. Earlier investigations of separated flow downstream from a rearward facing step, such as Eaton and Johnston (1981), studied the reattachment length of the flow following a step and demonstrated that the turbulent stresses are greatly reduced when the flow reattaches. Riesenthal et al. (1985) demonstrated that the flow can be significantly modified using time-periodic excitation that is applied either upstream or at the base of the step. Sigurdson (1995) considered the effect of azimuthally uniform time-periodic actuation on the separated flow on the surface of an axisymmetric blunt body downstream from its sharp leading edge (where the actuation was applied through a slot at the upstream edge).

Each jet in the azimuthal array is embedded into the surface with a 0.43 × 28.7 mm rearward facing orifice such that it is ejected over the constant radius Coanda surface that turns through ninety degrees. Vortical structures are formed at the edge of the actuator orifice by the motion of a diaphragm that is driven by a piezoelectric disk, which is mounted at the bottom of a sealed cavity. During the forward motion of the diaphragm the fluid is ejected from the cavity and the issued flow separates at the sharp edge of the orifice forming a vortex sheet that rolls into a vortex pair and is advected into the flow.

During the backward motion of the diaphragm air is drawn into the cavity. The previously ejected vortex pair is far enough away not be affected by the fluid drawn into the cavity. Therefore, while the net mass flux is zero, the synthetic jets produce a net momentum flux (Smith and Glezer, 1998). The piezoelectric disk is run at the resonance frequency of the cavity and the amplitude of the oscillation controls the increase in momentum flux introduced into the bulk flow (Smith and Glezer, 1998).

The effect of adjusting the angle of attack of an axisymmetric body concurrently with synthetic jet actuation was previously investigated by Rinehart et. al. (2003). The induced change in the aerodynamic force on the body at α = 0° was equivalent to the lift force at a 3° angle of attack. Actuation at a positive angle of attack decreased the efficiency of the synthetic jet and reduced the generated lift, ostensibly due to the upstream motion of the separation line, while a negative angle of attack increased the lift force.

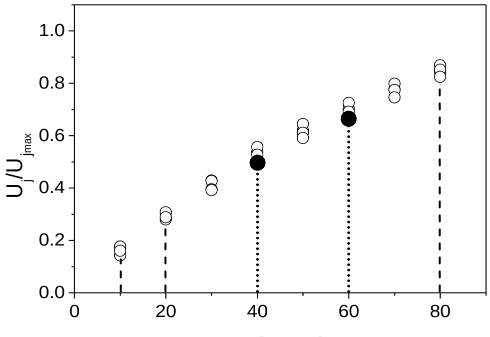

Figure 3.3. *Calibration of the jet exit velocities for four synthetic jet actuators with applied voltage. The nominal operating condition is 40Vrms for the model with control at the wake and 60Vrms, for the model with the mid-body cavity, the other conditions are 10, 20,and 80 Vrms.*

Both of the pairs of four synthetic jet actuators from both models are calibrated outside of the wind tunnel. The actuation frequency in the present experiments is 2 kHz and during calibration the actuation voltage is varied while the jet velocity is measured at the center of the orifice exit plane (the mean jet velocity is defined as averaged velocity during the expulsion half of the actuation cycle). Figure 3.3 shows the jet calibration data within the operating range of the present tests, having the jet strength operating conditions marked by the arrows (10, 20, 40, 60, and 80Vrms), where the default operating condition of the jet is 40 Vrms, $U_j/U_{j,max} = 0.45$, for the model with control at the wake, and 60 Vrms, $U_j/U_{j,max} = 0.7$, for the model with control upstream of the mid-body cavity. For a nominal wind tunnel speed of 40 m/s, and the corresponding $Re_D = 2.13\cdot10^5$, the momentum coefficient of each actuator in the default operating condition is $C_\mu = \frac{2\rho U_j^2 A_j}{\rho U_o^2 D^2 \pi/4} = 0.0013$, Where A_j is the actuator exit orifice area.

3.2 Wind Tunnel Model Frame Setup

The model is supported in the center of the wind tunnel test section by eight wires, 0.63mm in diameter, that are tied into a cylindrical (hoop) frame that is secured to the tunnel wall. As shown in Figure 3.4, the wires are connected to a frame that consists of two steel circular hoops that are each 3 mm thick and 48cm in diameter, placed 70cm apart using four aluminum rods (2cm in diameter) aligned along the tunnel length. Modified violin string keys are attached to the outside surface of the frame and are used to control the wire tension. The physical connection to the wind tunnel wall is facilitated through two 120 × 10 × 1cm steel beams connected horizontally along the left and right sides of the hoop frame. The wall connection is accomplished with four L-shape brackets each in line with vertical dampers, used to isolate the model from the tunnel vibration. Once the hoop frame is mounted in the wind tunnel, the tension in each of the mounting wires is set to 50N. The tension is measured using integrated force transducers, which are described Section 3.5.

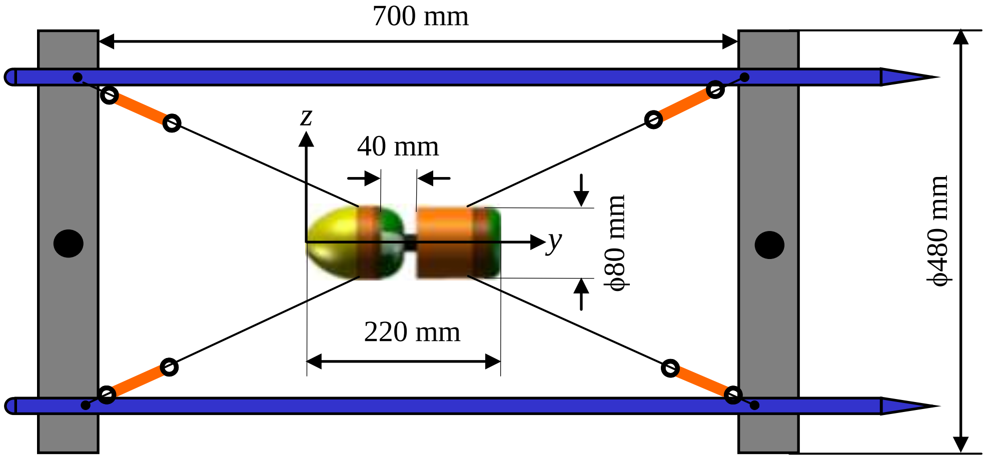

Figure 3.4. *Side view of the Mid-Body Cavity model mounted into the hoop frame and wire-support.*

The main reason for the use of a wire mounted model is to avoid mounting interference of a sting mount (e.g. Rinehart et. al., 2003). The effect of sting mount interference on drag measurements is described by Kurn (1968), who quantified the added drag on a bluff body. The mounting of wind tunnel models by wires is not new. In an earlier study Bennett (1978) used wire-mounted models to determine the oscillatory modes of the system for stability testing. His work focused on a scale F-14 model with 4 cables, and increased the tunnel speed until the lift produced by the wings balanced the model weight. Kiya et. al. (1990) used four piano wires to suspend a blunt axisymmetric body to study the axisymmetric separation bubble at the leading edge. Pressure probes were used to assist in the model's alignment. In a more recent work, Magill and Wehe (2002) used a wire suspended model for virtual flight testing of missile dynamics coupled with load cells to measure the tension. Their work involved 6 cables coupled to a circular ring mount placed around the model which enabled the measurements of the moments on the body.

3.3 Vibration Analysis

The axisymmetric body suspended in the hoop frame can be modeled as a spring-mass system, with a single central mass supported by eight springs. Each of the mounting wires has a longitudinal and a transverse vibration component. The longitudinal vibration is utilized to model each wire as a spring, and that vibration frequency is proportional to the cross sectional area of the wire and inversely proportional to the attached mass and the wire length (Roa, 1990),

$$f \approx \sqrt{\frac{A \cdot E}{m \cdot l}} = \sqrt{\frac{k}{m}} \tag{3.1}$$

Where m is the mass, k is the equivalent spring constant, A is the cross sectional wire area, l is the wire length, and E is Youngs Modulus of wire. In the present system, each wire is braided bronze which has a cross sectional area of $1.11 \cdot 10^{-6}$ m^2, a Youngs Modulus of 110Gpa, and a length of 0.33m. Therefore the equivalent spring constant is $3.7 \cdot 10^5$ N/m.

The suspended model has a configuration of,

$$(X + x, Y + y, Z + z)$$

$$\text{Where } x, y, z << X, Y, Z$$

Where X, Y, Z are the coordinates of the model about the cg, and x, y, z are perturbations in the three axial directions. The end points of the wires, connected to the hoop frame, are assumed to be rigid. During the small motions of suspended model, each of the springs (mounting wires) provides a restoring force (Roa, 1990),

$$\sum_1^8 \overline{F}_i = m\bar{a} = \sum_1^8 k\delta_i \tag{3.2}$$

Where $\bar{a} = \ddot{x}\,\bar{i} + \ddot{y}\,\bar{j} + \ddot{z}\,\bar{k}$, and $\delta_i = \delta_i(x, y, z, X, Y, Z, l)$

($\overline{F}$ is the restoring force, $\bar{a}$ is the model acceleration, m is the mass of the body, and δ is the wire displacement). All the wires are identical, ($k_1 = k_2 = k$) and symmetrical around the central body, having the same angle with respect to the three coordinate axes. Decomposing the forces into the three coordinate axes using geometry yields the following equations (3.3-3.5),

$$m\ddot{x} = 4k\cdot u_1\cdot\bar{i}\cdot\left[\left(\sqrt{(Y+y)^2+(X+x)^2+(Z+z)^2}-l\right)-\left(\sqrt{(Y-y)^2+(X-x)^2+(Z-z)^2}-l\right)\right] \tag{3.3}$$

$$m\ddot{y} = 4k\cdot u_2\cdot\bar{j}\cdot\left[\left(\sqrt{(Y+y)^2+(X+x)^2+(Z+z)^2}-l\right)-\left(\sqrt{(Y-y)^2+(X-x)^2+(Z-z)^2}-l\right)\right] \tag{3.4}$$

$$m(\ddot{z}+\bar{g}) = 4k\cdot u_3\cdot\bar{k}\cdot\left[\left(\sqrt{(Y+y)^2+(X+x)^2+(Z+z)^2}-l\right)-\left(\sqrt{(Y-y)^2+(X-x)^2+(Z-z)^2}-l\right)\right] \tag{3.5}$$

Where $l = \sqrt{X^2+Y^2+Z^2}$ and u_1,u_2, u_3 are the components of the unit vector, u, along the length of each wire.

Applying a first order Taylor expansion about (x_0, y_0, z_0),

$$f(x,y,z) \cong f(x_0,y_0,z_0) + f_x(x_0,y_0,z_0)\cdot(x-x_0) + f_y(x_0,y_0,z_0)\cdot(y-y_0) + f_z(x_0,y_0,z_0)\cdot(z-z_0)$$

$$\text{Where } (x_0, y_0, z_0) = (0,0,0) \tag{3.6}$$

Yields the following three equations,

$$\ddot{x} = \frac{8\cdot k.\cdot u_1}{m}(xu_1 + yu_2 + zu_3)\,\bar{i} \tag{3.7}$$

$$\ddot{y} = \frac{8\cdot k.\cdot u_2}{m}(xu_1 + yu_2 + zu_3)\,\bar{j} \tag{3.8}$$

$$\ddot{z} = \frac{8\cdot k.\cdot u_3}{m}(xu_1 + yu_2 + zu_3)\,\bar{k} - \bar{g} \tag{3.9}$$

The wires in the assembly of the model with tail actuators (Figure 3.1) each have a unit vector of $\bar{u} = 0.496\bar{i} + 0.712\bar{j} + 0.496\bar{k}$. The wires in the assembly of the second model (Figure 3.2) each have a unit vector of $\bar{u} = 0.526\bar{i} + 0.667\bar{j} + 0.526\bar{k}$. Using Matlab, the above equations 3.7-3.9 are solved numerically.

The natural frequencies in the (*x*, *y*, *z*) directions for the model with the tail actuators (mass 431 g), are (205Hz, 295Hz, 205Hz). For the model with a mid-body cavity (mass 900 g) the natural frequencies are (155Hz, 192Hz, 155Hz).

The actual vibration frequencies of the model were measured using the force transducers (Section 3.5) decomposed into the three coordinate axes. The natural frequencies in the (*x*, *y*, *z*) directions for the model with the tail actuators were (105Hz, 154Hz, 102Hz), and for the model with the mid-body cavity (86Hz, 110Hz, 85Hz). The difference in frequencies can be attributed to the mass of the models. The spectra from the force transducers from the model the tail actuators are displayed in Figure 3.5, where 3.5*a*, 3.5*b*, and 3.5*c* correspond to the lateral, vertical and longitudinal directions respectively.

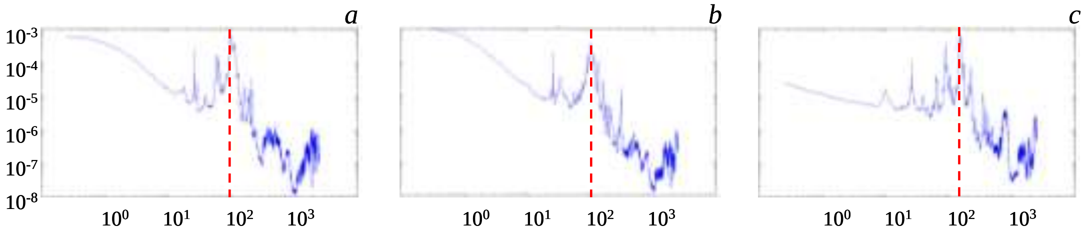

Figure 3.5. *Spectra taken from the force transducers for the model with control at the tail, normalized in the lateral direction, (a) vertical direction (b), and longitudinal direction (c) (x, z, y directions).*

The peaks at lower frequencies, particularly in the lateral and vertical directions (*x* and *z* directions) are caused by pitch and yaw moments of the model. For both cases the calculated frequencies are significantly higher than what is measured directly on the model. There are two reasons for the discrepancy. The first is the use of braided wire, which has many additional modes of vibration, compared to a uniform wire, and the second is that the mounting wires are able to move around their points of attachment. These additional modes of motion decrease the natural frequency of the system, similar to placing springs in series with one another (Roa, 1990).

In addition, laser vibrometer measurements are taken on the model with tail actuators in order to determine the amplitudes of the oscillations during the tunnel operation. The net displacements at $Re_D = 2.13 \times 10^5$ are found to be 0.11 mm, 0.07 mm and 0.065 mm in the in the lateral, longitudinal, and vertical (x, y, z) directions respectively.

The transverse vibration of each wire, can be neglected when the wire mass is negligible compared to the central mass (Roa, 1990). The wire tension, which is a function of the transverse vibration, is therefore independent of the system. The transverse vibration frequency is (Roa, 1990),

$$f = n\frac{1}{2L}\sqrt{\frac{T}{\mu}} \tag{3.8}$$

Where T is the wire tension, L is the wire length, μ is the linear mass of wire, and n is the harmonic vibration number. In the wire mounting application, T = 50N, μ = is 0.006 kg/m, and L = 0.27 m, yielding a first harmonic frequency of 169 Hz. As the transverse frequency of the wires is within the same order of magnitude of the natural frequencies of the system, this implies that in the present setup it may not have been a fully appropriate to assume only uniaxial wire vibration and neglect the transverse motion. Clearly, the system involves complex motions that deserve a more substantial follow up. A similar discussion of the vibrations in a wire mounted system is presented in Magill and Wehe (2002).

3.4 Flow Diagnostics

The primary method of the flow characterization is Particle Image Velocimetry (PIV). The flow is seeded with smoke particles and illuminated with a double pulse 50mJ Nd: YAG laser. The image pairs are captured using a 1008 × 1016 Pixel CCD camera. The magnification of the view depended on the plane of view, and varied between 60 and 65 µm/pixel. The PIV camera is mounted on a two-axis computer-controlled traversing mechanism outside the wind tunnel, so that multiple fields can be captured phase-locked to the actuation waveform and subsequently combined to yield a larger view of the flow. In the present work, the "full" flow field is mapped using four individual, partially overlapping PIV images that span the domain from upstream of the jet orifice to $y/R \approx 2.8$ and $z/R \approx -2.4$ to 0.5 (Figure 3.6*a*). For the model with the mid-body cavity, a single PIV field is taken within $y/R = -0.2$ to 1.25 with respect to the top jet orifice, over the entire cavity (Figure 3.6*c*). The PIV measurements are used to compute the vorticity and turbulent kinetic energy.

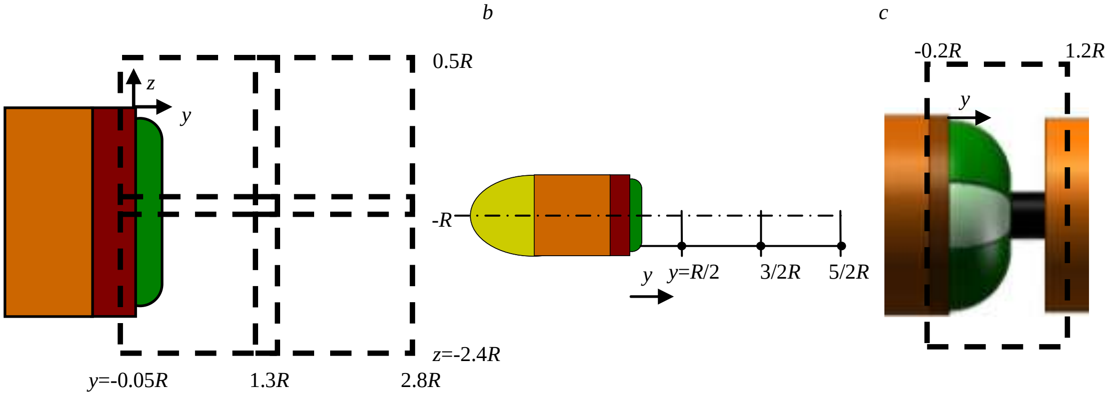

Figure 3.6. *Fields of view for PIV at the model wake (a), hot-wire measurements in the wake (b), and PIV in the mid-body cavity (c).*

Hot wire anemometry measurements were taken in the wake of the model, for the model with control at the tail, in order to map out and characterize the flow behind the body. The hot wire probe is held on a 2D traverse behind the model and is calibrated *in situ*. These measurements yielded the RMS fluctuations of the streamwise velocity and spectra in the separated shear layer and wake core. The measurements were taken over a 22 × 22 points grid across the wake measuring $1.1R \times 1.1R$, at $y/R = 0.55$, 1.5, and 2.45, where y is measured from the downstream edge of the model, as seen in Figure 3.6*b*.

3.5 Force Measurement

3.5.1 Force Sensors

The time dependent tension in each of the mounting wires was measured and used to extract the aerodynamic forces and moments on the model. These measurements were accomplished using an in line sensor comprised of four strain gages. The resistance of the strain gage wire is

$$R = \frac{\rho l}{A} \tag{3.9}$$

where ρ is material resistivity, l is the gage wire length, and A is the wire cross sectional area. The use of direct force measurements using in line strain gages has been previously investigated. Bennett et. al. (1977) used four cables in line with strain gage load cells, to suspend a scale model of an F-14 aircraft. Similarly Magill et. al. (2004) used a six wire system to suspend a missile within a wind tunnel using a strain gage collar at the base of the wires to record the varying tension, to calculate the forces and moments on the body.

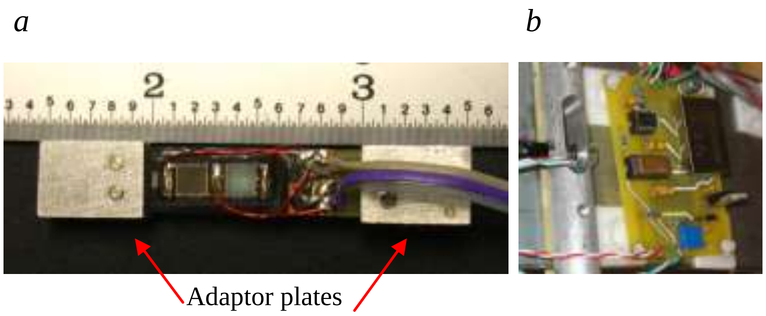

Figure 3.7. *Custom-made force-measurement transducer (a) and its detached circuitry (b).*

The circuitry used for the measurements includes a Wheatstone bridge amplifier where the sensor (Figure 3.7*a*) and the amplifier (Figure 3.7*b*) are separate. The four arms of the Wheatstone bridge are formed with two Tee-Rosette strain gages. Each Tee-Rosette incorporates two normal strain gage sensors, each having a resistance 1KΩ. The strain gages are placed on opposite sides of an FR4 circuit board of dimensions 15 × 8 × 1mm. The board is placed in series with the mounting wires using two adaptor plates and set screws shown in Figure 3.6*a*. Each sensor is attached at the anchoring point of the support wires. The Rosettes are connected such that each pair of parallel lined gages is connected on opposite arms of the Wheatstone bridge. Rosette 1 incorporates strain gages, S1 and S2 and Rosette 2 incorporates strain gages S3 and S4 as shown in Figure 3.8*a*. Therefore, the change in tension of the mounting wires results in a change in resistance of S1 and S3, whose traces run parallel with the mounting wires, and no change in S2 and S4. In this setup, all four arms of the bridge experience the same change in resistance caused by temperature variations. Therefore, it is expected that that the voltage output is independent of temperature and this is discussed in more detail in the next section.

The amplifier circuit is shown schematically in Figure 3.8*b*. Strain gage S4 is placed in parallel with a 50KΩ balance limiting resistor and a 50KΩ potentiometer, providing the ability to zero the voltage of each transducer after pre-tension is applied. The input power supply is first run through a DC-DC converter to produce power outputs of +12V and -12V required for the two op-amps in the circuit. The first op-amp is an AD254 chip and is designed to have a gain of 2000. The second is a non-inverting op-amp with a gain of 2. Once connected to the data acquisition board, the signals go through a 50% voltage divider, resulting in an overall circuit gain of 2000.

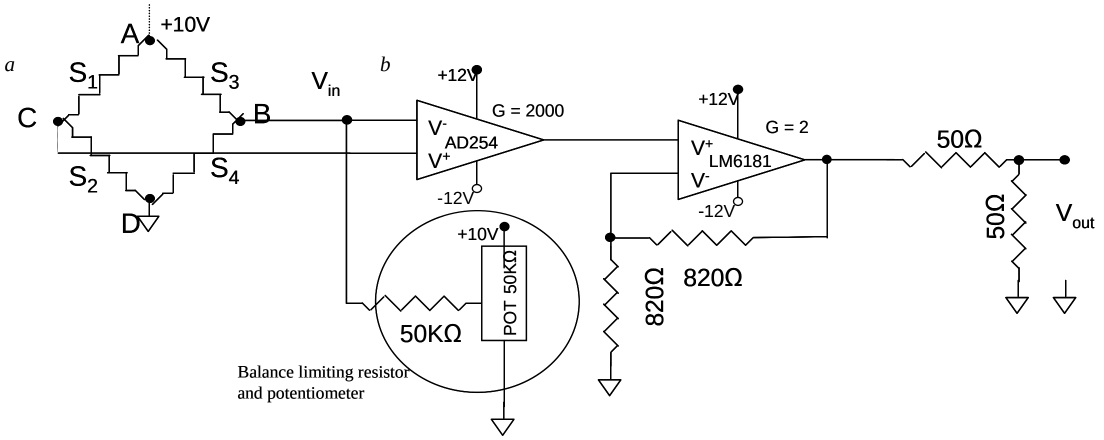

Figure 3.8. *Circuit schematics of force transducer, Wheatstone Bridge (a) and Amplifier circuit (b).*

3.5.2 Transducer Temperature Calibration

The heat generated by each of the strain gages during operation, (~ 25 mW) result in slight changes of the resistivity of the conductive wire. Therefore, small fluctuations in the resistance across each strain gage occur with drift in laboratory temperature, which changes the rate of convection heat transfer. The construction of the Wheatstone bridge minimizes the circuit's sensitivity to temperature drift. Figure 3.9 illustrates the temperature sensitivity of the sensor module for a given flow condition in the wind tunnel. The sensors' readings have a typical sensitivity of about 0.03 – 0.04 V/°C, which is a five fold reduction compared to a Wheatstone bridge only partially constructed of strain gages. A temperature compensation algorithm, much like the temperature compensation procedure for hot-wire anemometry, is incorporated into the raw signal processing routine.

When the tunnel is operated for approximately one hour, the laboratory reaches a nearly steady-state temperature at around 29° C ± 1° C and the temperature calibration typically starts at about 27° C. All the transducers' voltages are sampled while the tunnel speed is held constant at 40 m/s. As the temperature increases, the transducers' voltages increase, and a family of calibration data sets is acquired as shown in Figure 3.9. The measured slope for each sensor is used to compensate for temperature changes. The temperature calibration procedure is repeated at the beginning of each test day, following an initial warm-up of the tunnel.

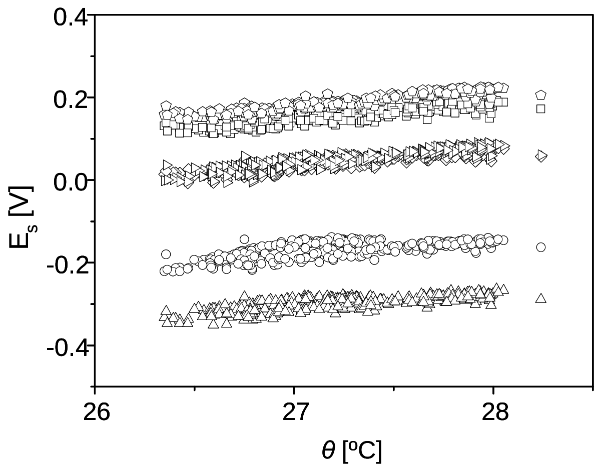

Figure 3.9. *Temperature sensitivity of the transducers' response* E_s *for* $Re_D = 2.13 \cdot 10^5$. *Each of the symbols represent a different transducer.*

3.5.3 Force and Moment Calculation and Calibration

Each of the force measurements of the individual transducers is decomposed into three coordinate axis and the three orthogonal forces, drag F_D, lift F_L, and side force F_S are obtained by the directional sum of the eight decomposed forces along the wires. The moments are calculated by taking sum of the cross products between the position vector $\bar{r}$ between the model's center of gravity (cg) and the connection point of each wire, and the force along each wire (all the axes pass through the central axis of the model). The roll moment cannot be resolved, and the pitch, M_P and yaw, M_Y are extracted.

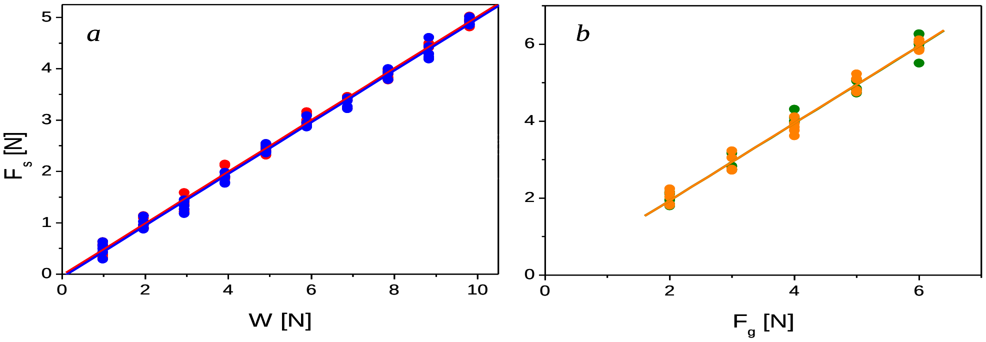

Figure 3.10. *Static validation of the transducers' force measurement F_s split into the tension (●) and compression (●) responses to static weight W (a), and as a function of the applied force F_g to the front (●) and back (●) (b).*

Each force transducer is calibrated prior to assembly, on the bench, independently with precision masses, yielding the variation of linear load with voltage for each. These measurements are conducted by suspending each transducer in a miniature wind tunnel to limit changes in temperature. Initially a common large mass is hung under each transducer to apply pre-tension. Following this, the output voltage is sampled as masses, up to 2kg, in increments of 100 g, are applied to each transducer. These calibrations verified that the transducers' responses were all within 3% of each other. Once the transducers were incorporated into the suspended model support frame, a separate set of calibration procedures are conducted. First, precision masses are hung on the model for additional *in situ* sensor calibration. These tests demonstrated a linear scale of about 170 mV/N for all the transducers, which is very similar to the a priori calibration. Each of the measurements is split into responses for compression (i.e., reduced tension) and for tension that are shown in Figure (3.10*a*). These data indicate that the transducers respond to both tension and compression in the same way. These calibration curves are used not only for data reduction but also during the mounting, alignment, and balancing of the wind tunnel model within the hoop frame. A second set of *in situ* calibration involves testing of the transducers responses to the static force applied along the body's main axis, at the front (nose) and at the back (tail) of the model using a 10 Newton gauge, and responses of the force transducers are shown in Figure (3.10*b*). Again, the force measurement algorithm is validated in these tests as well.

CHAPTER 4

Fluidic Control of the Wake

This chapter presents the results of experiments in which fluidic control is applied at the model's tail section. The flow control approaches that are tested include continuous actuation by a single and multiple jets, amplitude modulation of the jet driving signal, and actuation of the jets in a sequential pattern around the tail of the model. For each case, the changes in the aerodynamic forces induced by the actuation are measured relative to the corresponding forces in the baseline (unforced) flow. Furthermore, the resulting flow dynamics in the wake is characterized by the PIV and hot-wire anemometry.

4.1 Actuation by a Single Jet

The variation of the magnitude of the normal force coefficient C_N induced by a single (top) actuator with C_μ is shown in Figure 4.1 for three global Reynolds numbers $Re_D \times 10^{-5}$=1.06, 1.6, and 2.13. The present results are in agreement with the earlier measurements of Rinehart et al. (2003): for a given Re_D, the induced force first increases rapidly with C_μ of the control jet, and then the rate of increase diminishes, and C_N ultimately becomes invariant with C_μ for $C_{\mu sat} > 0.001$. Furthermore, the saturation value of C_μ is independent of the tested Re_D. This suggests that there is a limiting ΔC_N that can be achieved for a fixed tail model geometry.

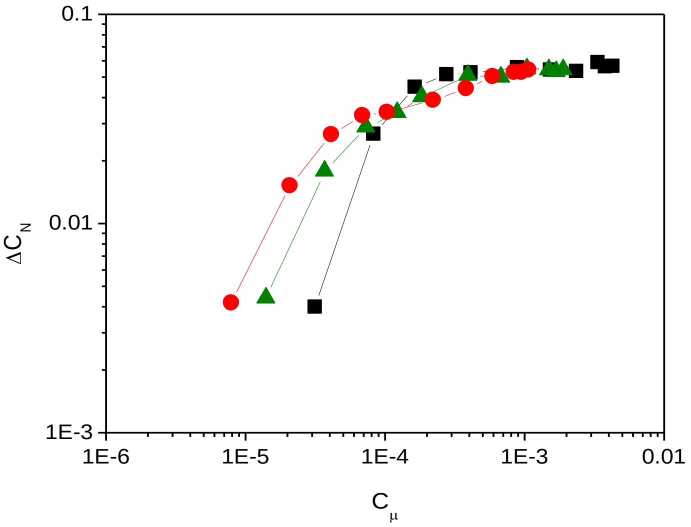

Figure 4.1. *Variation of the ΔC_N with jet momentum coefficient effected by a single actuator at $Re_D \times 10^{-5}$ = 1.06 (■), 1.6 (▲), and 2.13 (●).*

The connection between the apparent "saturation" of the generated normal force and the corresponding flow vectoring over the model tail is assessed using ensemble-averaged PIV measurements in a vertical plane that intersects the center of the slit of the active jet actuator (the top jet). These measurements are taken for the baseline flow, and in the presence of actuation at several levels of C_μ and $Re_D = 2.13 \times 10^5$. Figure 4.2 shows raster plots of the mean vertical velocity component V. The baseline flow (Figure 4.2*a*) separates at the tail step and the ensuing shear layer remains nearly-horizontal in the near field and the direction of the outer flow is not altered significantly. The cross stream velocity above the unforced shear layer is virtually zero. As the actuation is applied, the vectoring of the cross flow becomes stronger with C_μ. It is remarkable that even though the force measurement (Figure 4.1) shows only marginal increase in the induced force between $C_\mu = 4.8{\cdot}10^{-4}$ and $1.1{\cdot}10^{-3}$, there is clearly a significant increase in the degree of flow vectoring between Figures 4.2*e* and 4.2*f*. This suggests that the saturation is connected with three-dimensional effects near the edges of the jet orifice that may offset the effects induced at the centerline.

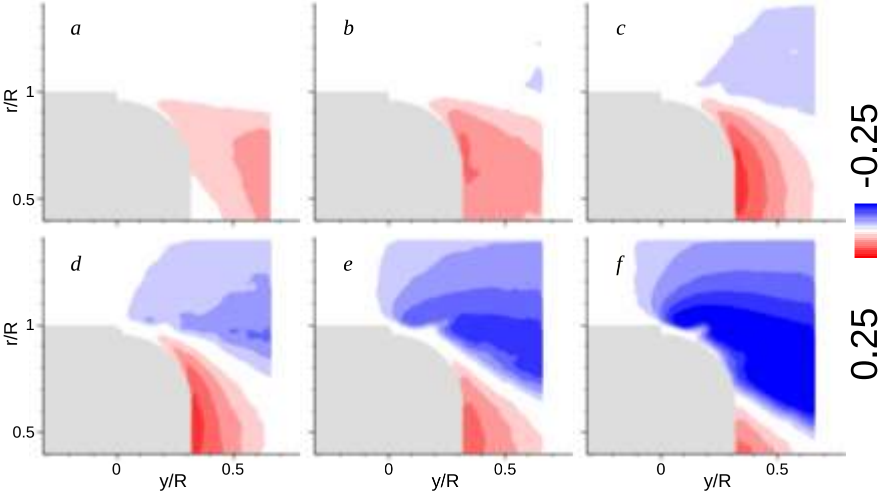

Figure 4.2. *Raster plots of the radial velocity component V/U_0 for the baseline flow at $Re_D = 2.13 \times 10^5$ (a) and the flow actuated by the top jet at $C_\mu = 2.1 \cdot 10^{-5}$ (b), $6.9 \cdot 10^{-5}$ (c), $2.2 \cdot 10^{-4}$ (d), $4.8 \cdot 10^{-4}$ (e), and $1.1 \cdot 10^{-3}$ (f).*

The structure of the near wake behind the model is characterized using hot-wire measurements. Before assessing the effects of actuation on the wake dynamics, the baseline wake is characterized in the absence of actuation at $Re_D = 2.13 \cdot 10^5$. Distributions of the time-averaged streamwise velocity and the corresponding RMS velocity fluctuations in the *x*-*z* plane are shown in Figure 4.3 at three streamwise stations $y/R = 0.55$, 1.5, and 2.45. These distributions show that the baseline wake in the near field (Figures 4.3*a* and 4.3*d*) has a nominal four-fold symmetry. The presence of lobes in the wake is attributed to interactions with the wakes of the support wires (at the azimuthal centers of the high velocity depressions) and the formation of pairs of counter-rotating streamwise vortices at the juncture of the wires and the body. Farther downstream (Figures 4.3*c* and 4.3*f*), the near wake becomes more axisymmetric as the shed vortices lose their coherence. The accompanying maps of the RMS velocity fluctuations exhibit higher levels of turbulent fluctuations within the separated shear layer at $y/R = 0.55$ (Figure 4.3*d*), which spread towards the wake core in downstream direction, as an indication of increased mixing. Therefore, the most uniform RMS distribution is measured at the farthest downstream location ($y/R = 2.45$, Figure 4.3*f*). Furthermore, hot wire spectra in the wake indicate that the "natural" shedding frequency of the model is around 120 Hz, which corresponds to $St_D = 0.24$.

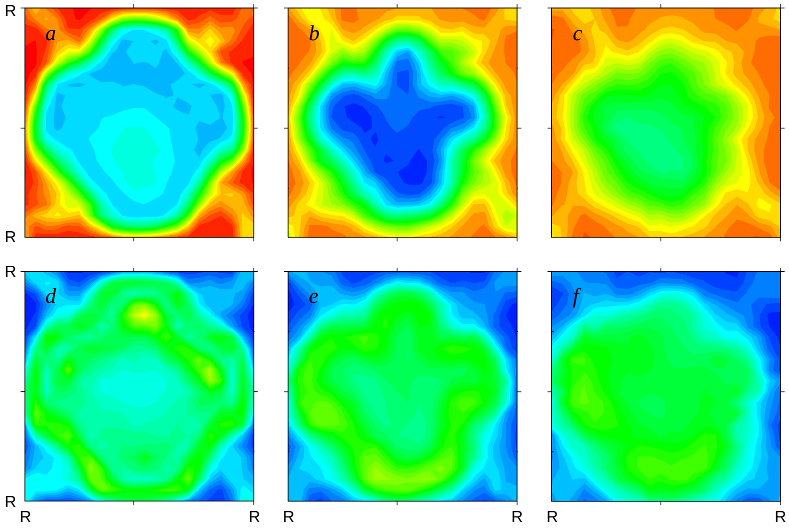

Figure 4.3. *Contour maps of the mean velocity field (a – c) and the RMS velocity fluctuations (d – f) for the baseline flow at y/R = 0.55 (a, d), 1.5 (b, e), and 2.45 (c, f).*

The corresponding flow field in the presence of actuation (top actuator, $C_\mu = 1.5 \cdot 10^{-3}$) is shown in Figure 4.4. The wake in the presence of actuation is reasonably symmetric about the *y* axis and, as expected, the actuation vectors a segment of the outer flow above the top actuator towards the center of the wake and leads to a slight downward deflection of the entire wake. When compared to corresponding maps in Figure 4.3, it is clear that there is a local reduction in the wake deficit, particularly around the azimuthal center of the actuator's orifice. This effect is visible in maps of the streamwise velocity distributions in Figures 4.4*a* ($y/R = 0.55$), and *b* ($y/R = 1.5$), where the wake develops two symmetric low velocity lobes that are separated by higher-speed fluid from above. The presence of these low-speed domains is also evident from the RMS maps in Figures 4.4*d* and *e*. The vertical deflection of the entire wake is clearly evident in Figures 4.4*c* and *f* (y/R = 2.45) and is estimated to be z/R = 0.25. As shown by Abramson et. al. (2007), the actuation transports CW vorticity all the way to the base of the model and leads to the formation of a thin boundary layer on the base before the flow separates into the deflected near wake.

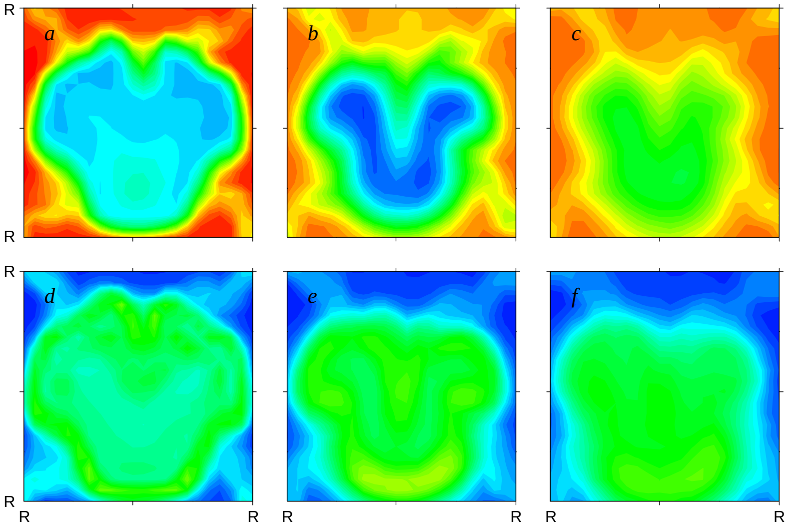

Figure 4.4. *Contour maps of the time-averaged axial velocity field (a – c) and the RMS velocity fluctuations (d – f) for the flow controlled by the top actuator at y/R = 0.55 (a, d), 1.5 (b, e), and 2.45 (c, f) at* $C_\mu = 1.5 \cdot 10^{-3}$.

Power spectra of velocity fluctuations measured in the presence and absence of actuation at two cross-stream elevations (corresponding to the upper shear layer and at the center of the wake) of each of the three streamwise measurement stations, y/R = 0.55, 1.5, and 2.45, are shown in Figure 4.5 (spectra of the unactuated flow are also shown for reference). The spectra in Figures 4.5*a-c* are measured at the upper shear layer of the wake (z/R = 1), and the spectra in Figures 4.5*d-f* are measured at the wake core (z/R = 0), both at *yR* = 0.55, 1.5, and 2.45. At *y/R* = 0.5 (Figures 4.5*a* and *d*) the baseline shear layer is dominated by the large-scale motions below 1kHz, while the motions within the wake core exhibit a wider range of scales with significant energy content, indicating the effect of a base "bubble" and the merging of the separated shear layers. Upon actuation, the energy associated with the large-scale motions within the wake shear layer decreases and induced high-frequency mixing by the actuation leads to energy transfer to the higher spectral components with an emergence of an inertial subrange that also includes a spectral peak at the actuation frequency at 2 kHz.

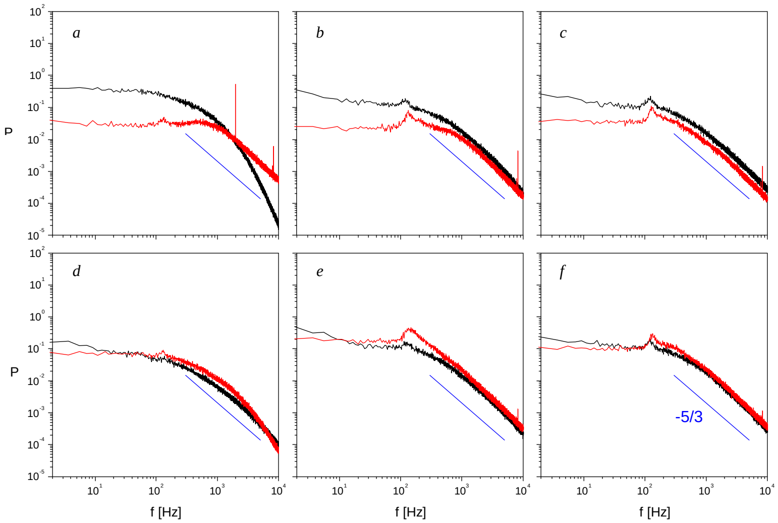

Figure 4.5. *Power spectra of the velocity fluctuations at the upper shear layer (a-c) and the wake core (d-f) for the baseline (▬) and the flow actuated by the continuous top jet (▬) at y/R = 0.55 (a, d), 1.5 (b, e), and 2.45 (c, f).*

Although not as prominent, some of the effects of the actuation are also evident within the wake core (Figure 4.5*d*), where decrease in energy of the large scale motions is also accompanied with an increase of energy of the small scales. At the other two streamwise measurement locations (*y*/*R* = 1.5 and 2.45), all baseline spectra exhibit an inertial subrange and a broad peak at about 120 Hz, which corresponds to St_D = 0.24 and appears to be the natural shedding frequency of the model. While the spectral energy within the shear layer exhibits a broadband decrease (Figure 4.5 *b* and *c*), motions at the wake core become energized in a band about the spectral peak at f = 120 Hz, accompanied with decrease of energy of the larger scales (Figure 4.5 *b* and *c*). These spectral distributions indicate that the effect of actuation rapidly spreads towards its center, even though the actuation is located at the wake's periphery. It is also noted that the baseline spectral peak at 120 Hz changes to 130 Hz and a somewhat higher frequency within the wake core under the actuation. These changes may be attributed to the distortion of the near wake by the actuation (Figure 4.5*b*).

The changes in the aerodynamic forces induced by the actuation are measured relative to the corresponding aerodynamic forces of the unactuated flow. The data records are typically 4.5 seconds long, the actuation is turned on at $\tau = 0.5$ sec and terminated at $\tau = 2.5$ sec, corresponding to 4,000 actuation cycles. This approach allows for measurements of the transitory aerodynamic forces during the onset and termination of the actuation, as well as the "quasi-steady" response once the actuation transients die out. The aerodynamic forces and moments are initially investigated in the absence of actuation. The flow-induced drag, lift, and side force (F_D, F_L, and F_S) and pitch and yaw moments (M_P, and M_Y), are measured using the in-line force sensors (Section 3.5). The RMS fluctuations in the force traces are 0.05 N and in the moments are 0.002 N·m over the 4.5 second set. Spectral analysis of the time traces (not shown) for the individual forces and moments yields peaks of the corresponding vibration modes. Although the oscillation amplitude is small, the resonance frequencies for the drag, lift, and side force are 154, 102, and 105 Hz respectively (discussed in more detail in Section 3.3) and for the pitch and yaw moments are measured at 30 and 27 Hz.

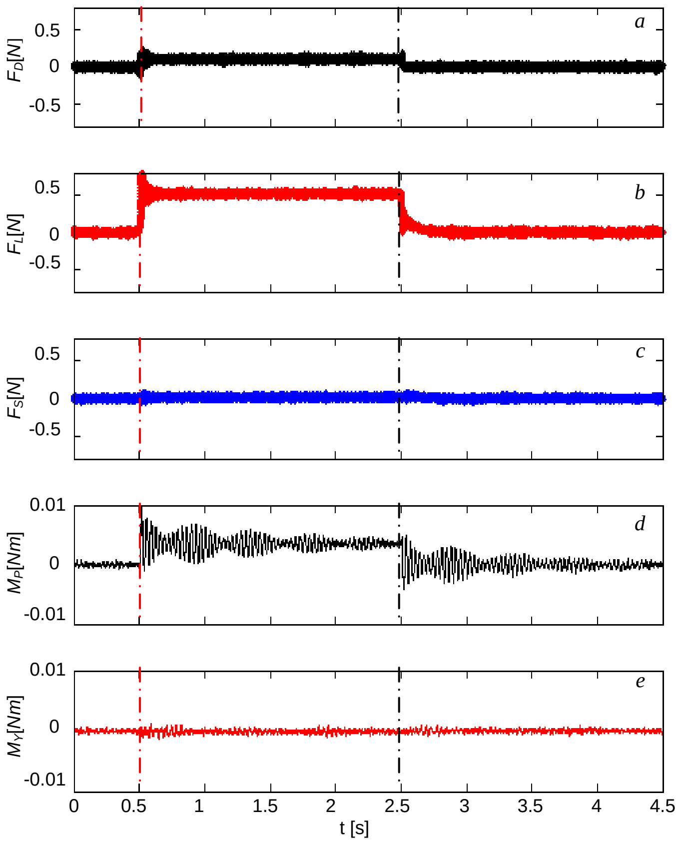

Figure 4.6. *Time traces of the changes in drag (a), lift (b), and side (c) forces, and in the pitch (d)and yaw (e) moments when the flow is actuated by the top jet* $C_\mu = 1.5 \cdot 10^{-3}$

Continuous actuation by a single top jet results in the vectoring of the shear layer and free stream flow over the Coanda surface into the models' near wake, generating a normal force. The measured phase-averaged forces and moments generated by actuation of the top jet are shown in Figure 4.6 for $C_\mu = 1.5 \cdot 10^{-3}$. These data show that the segmented vectoring of the flow on the Coanda surface yields a resultant vertical (lift) force that is nominally 0.5 N (C_L = 0.043 based on the free stream velocity and model platform area). Along with the change in the vertical force, there is also an increase in the counterclockwise pitching moment (relative to the cg) corresponding to a nose-down moment. The induced pitching moment increment remains virtually invariant during the actuation period. It is noteworthy that along with the change in the lift force, there is also an increase in the drag force of about 0.1N. Although the partial vectoring and closure of the wake segment by the active top actuator leads to a reduction in drag, it is offset by an increase in drag due to the induced force on the Coanda surface. A similar increase in induced drag on an airfoil with an adjustable trailing edge Coanda surface was also reported by Englar (2000). Each of the force and moment increments exhibits transient effects owing to the onset and termination of the actuation. There are two distinct time scales associated with these transients. The first, fast time scale is the characteristic rise (or fall) time that is typically on the order of $5T_{conv}$ (or $10T_{conv}$) where T_{conv} = 3.75 msec is the convective time scale over the model. It is interesting to note that the fall time is longer as a result of the flow detachment from the Coanda surface. The second, slower time scale is the settling time which is associated with the decay of the oscillations that are excited at one of the natural frequencies of the model. For example, the drag force (Figure 4.6*a*) oscillates at 155 Hz during the transient onset and the full actuation effect is established within $32T_{conv}$. This lengthy settling time is associated with the dynamics of the entire model and mounting wires. Interestingly, the settling time of the drag force upon termination of the actuation is considerably shorter ($7T_{conv}$) ostensibly as a result of the dissipation or damping associated with the separation of the flow over the actuated segment. The settling time following the actuation onset of the lift force (Figure 4.6*b*) is about $48T_{conv}$ and is associated with the lower natural oscillation frequency in the vertical direction (about 100 Hz). It is remarkable that compared to the drag transient that is associated with the termination of the actuation, the corresponding transient for the normal force is considerable longer (about $58T_{conv}$) indicating lower damping for model oscillations in the vertical (*y*-*x*) plane as is also evident from the oscillations in the pitch increment in Figure 4.6*d*.

4.2 Actuation by Multiple Jets

Actuation by multiple jets can lead to augmentation and redirection of the induced aerodynamic forces. The variation with jet Reynolds number of the forces induced by several programs is shown in Figure 4.7. The change in force induced by a single jet actuator corresponds to the data shown in Figure 4.1. When two adjacent jets are active there is a consistent increase in the induced normal force ΔC_N with possible saturation at the highest Re_j. Since the maximum ΔC_N is close to a vector addition of the two orthogonal components that would each be induced by a single jet, it may be concluded that there is little or no interference between the actuators. In the case of simultaneous actuation by three jets, it may be expected that the resulting lift force does not differ much from single-jet actuation. This appears to be the case at higher Re_j, but ΔC_N is lower than the force induced by a single jet at lower Re_j, ostensibly as a result of an imbalance between the jet actuators at the lower Re_j. Finally, actuation by all four jets is expected to induce no net force, which deviates somewhat at intermediate actuation levels because of slight variations between the actuators.

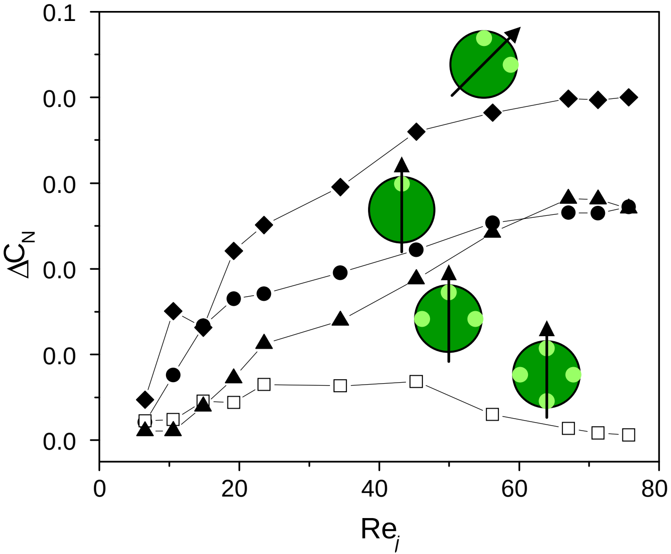

Figure 4.7. *Relative change in the* ΔC_N *at different* Re_j *at* $Re_D \times 10^{-5} = 2.13$*, and one (●), two (♦), three (▲), and all four jets active (□)*

Measurements of the velocity field in the near wake of the model are obtained using four partially-overlapping PIV fields as described in section 3.4. Figures 4.8*a*-*f* show the time-averaged velocity and vorticity distributions and 2-D estimates of the turbulent kinetic energy (TKE) k for the baseline and controlled flows ($C_\mu = 1.1 \cdot 10^{-3}$, $Re_D = 2.13 \cdot 10^5$). The near-wake data of the baseline flow show a recirculating domain up to about $y/R \approx 2$. It is also evident that the baseline (Figures 4.8*a* and *d*) is slightly asymmetric which is particularly noticeable in the distributions of the TKE where higher levels are measured at the lower shear layer. As the top actuator is activated, there is a significant vectoring of the upper shear layer, suppressing the recirculation near the top edge of the wake (Figure 4.8*b*). The actuation transports CW vorticity all the way to the base of the model and leads to the formation of a thin boundary layer with opposite vorticity on the base surface. The vectoring is accompanied by the enhanced TKE in the lower shear layer (Figure 4.8*e*) with substantially lower levels in the vectored layer segment. Upon concomitant actuation by the top and bottom jet, as shown in Figures

4.8*c* and *f*, the wake becomes nearly symmetric and the stagnation point moves inward towards the body to $y/R \approx 1.5$. It is noteworthy that the peak TKE coincides roughly with the centerline stagnation point.

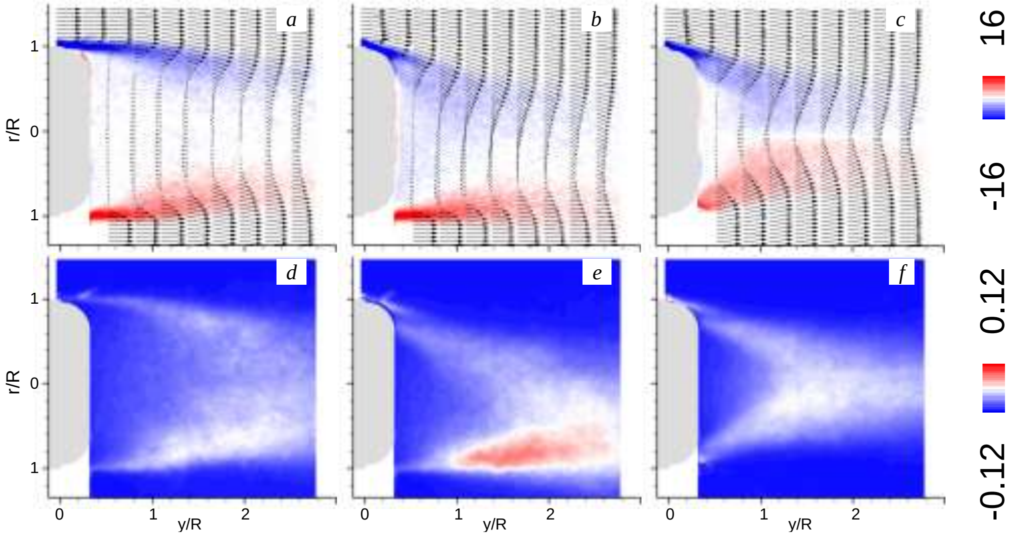

Figure 4.8. *Raster plots of the mean vorticity component* ζ^* *with overlaid equidistant mean velocity profiles (a, b, c) and turbulent kinetic energy k (d, e, f) for the baseline flow at* $Re_D = 2.13 \times 10^5$ *(a, d) and the flow actuated by the top (b, e) and both top and bottom actuators (c, f) at* $C_\mu = 1.1 \cdot 10^{-3}$.

Direct comparison of the actuation by the top, and both the top and bottom jets, relative to the mean baseline flow is further analyzed in Figure 4.9. Cross-stream distributions of the time-averaged normalized velocity components (U^* and V^*), vorticity (ζ^*), and turbulent kinetic energy (k^*) corresponding to the raster plots in Figure 4.8 are shown at three streamwise locations (y/R = 0.5, 1.25, and 2.75). In the absence of actuation, the near wake is nominally axisymmetric and the velocity deficit on the centerline increases somewhat between y/R = 0.5 and 1.25. The presence of symmetric (top and bottom) actuation leads to symmetric streamwise velocity distributions and the velocity deficit near the edges of the top and bottom shear layer segments is diminished indicating tilting of the outer flow towards the near wake. It is noteworthy that the cross stream velocity distribution shows evidence of strong symmetric recirculation at $y/R = 0.5$ (Figure 4.9*b*) which diminishes at the next streamwise station (Figure 4.9*f*). The wake becomes asymmetric and the velocity deficit near its upper edge is reduced when the top actuator is activated (Figures 4.9*a*, *e*, and *i*). The strong asymmetry is also evident in distributions of the cross stream velocity which at $y/R = 1.25$ (Figure 4.9*f*) is predominantly downward with peak $|V/U_0| \approx 0.45$. At the farthest downstream location ($y/R = 2.75$, Figure 4.9*i*), the wake does not exhibit reversed flow and the velocity deficit is substantially reduced ($U^* \approx 0.5$). It is also evident that the tilting of the flow exceeds the bottom edge of the measurement domain. The distinct peaks of the cross stream distributions of vorticity in the baseline flow (Figures 4.9*c* and *g*) exhibit peaks within the shear layer segments and negligible levels of vorticity elsewhere. These peaks diminish near the active actuators owing to the mixing induced by the actuation. By $y/R = 2.75$ (Figure 4.9*k*), all vorticity levels are about order of magnitude lower than at the first streamwise location, and no significant changes are seen in the actuated flows. Finally, cross stream distributions of the turbulent kinetic energy (TKE) at $y/R = 0.5$ are shown in Figure 4.9*d*. The baseline flow exhibits weak narrow peaks within the shear layer segments and lower levels across the wake and the actuation leads to small increases in the TKE levels. The effects of actuation on the TKE are more prominent at $y/R = 1.25$. While symmetric actuation leads to a strong increase in TKE at the center of the wake, asymmetric actuation leads to significant increases in TKE in the shear layer segment on the opposite side of the wake ostensibly as a result of the strong downwash which is evident in Figure 4.9*f*.

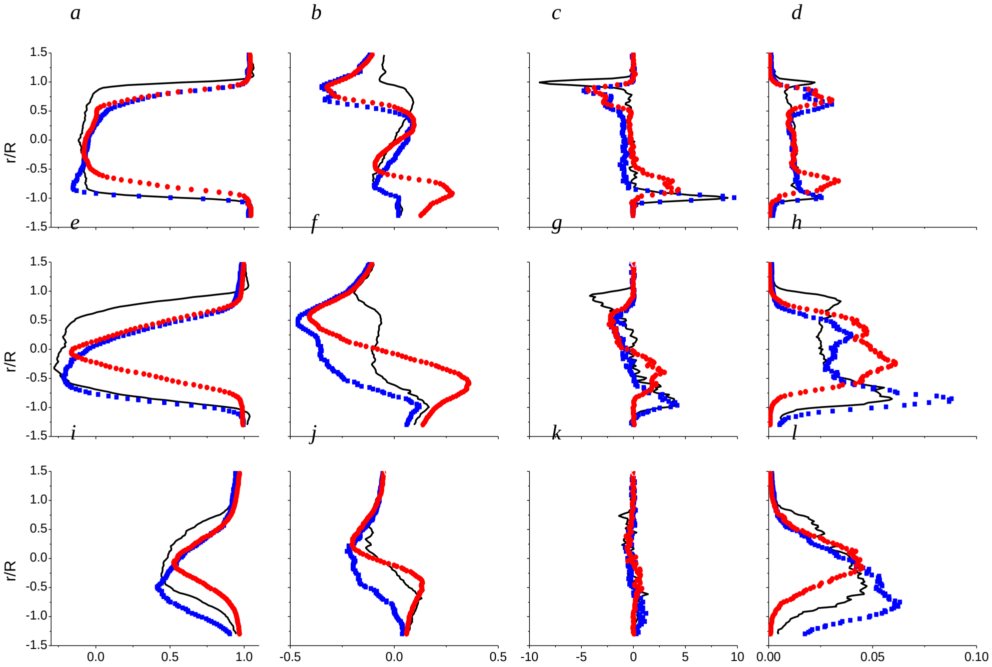

Figure 4.9. *Profiles of the U* (a, e, i), V* (b, f, j), ζ* (c, g, k), and k* (d, h, l) at y/R = 0.5 (a-d), 1.25 (e-h), 2.75 (i-l), for the baseline flow at* $Re_D = 2.13 \times 10^5$ *(—) and the flows actuated by the top (■) and both top and bottom jets (●) at* $C_\mu = 1.1E\text{-}3$.

The structure of the wake due to the combined actuation of two adjacent jets (top and left) is mapped using hot wire anemometry (Figure 4.6, $C_\mu = 1.5 \cdot 10^{-3}$ and $Re_D = 2.13 \cdot 10^5$). The local vectoring of the separated flow towards the center of the wake and the formation of two lobes is seen in Figure 4.10*a*, and it intensifies in Figure 4.10*b*. Figure 4.10*c* shows the deflection of the wake along the line of symmetry between the actuators, in the bottom right direction. It is noteworthy that the distortion of the baseline flow leaves a narrow strip between the actuators where the deflection of the flow is smaller, indicating a gap between the two actuators. Furthermore, it should be pointed out that just as in the planar PIV measurements shown in Figure 4.8*e*, the hot-wire measurements indicate that the peak fluctuating energy is excited in the wake's shear layer opposite of the actuation source as evidenced by the peak RMS velocity fluctuations in Figure 4.10*e*.

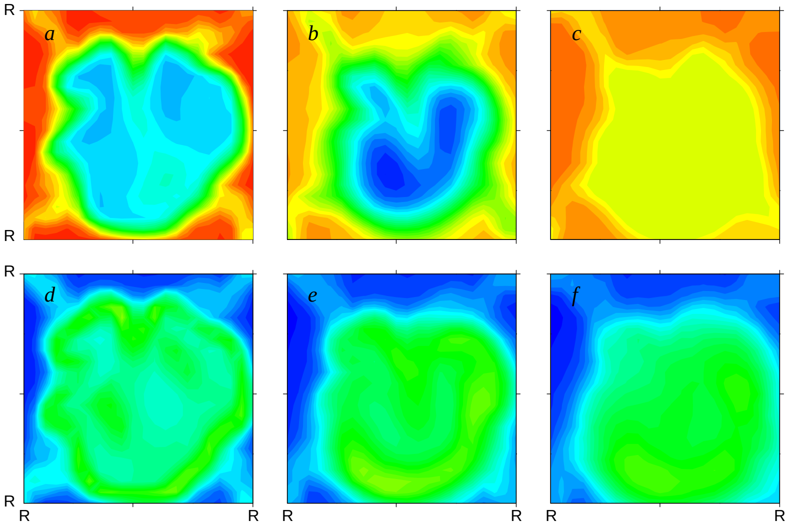

Figure 4.10. *Contour maps of the mean velocity field (a – c) and the RMS velocity fluctuations (d – f) for the flow controlled by the top and left actuators at y/R = 0.55 (a, d), 1.5 (b, e), and 2.45 (c, f).*

The time traces of the resulting changes in the forces and moments associated with concomitant actuation by the two adjacent jets (top and left) are presented in Figure 4.11($C_\mu = 1.5 \cdot 10^{-3}$ and $Re_D = 2.13 \cdot 10^5$), using the same time-history as shown in Figure 4.6. It is shown that when the two adjacent jets are active, the yielded forces and moment increments are additive. The increment in both lift and side forces is about 0.5 N (Figures 4.11*b* and 4.11*c*), the resulting force magnitude is about 0.7 N ($C_L = 0.06$) and is aligned in the radial direction midway between the two active jets. Since the maximum ΔC_L is close to a vector addition of the two orthogonal components that would each be induced by a single jet, it may be concluded that there is little or no interference between the actuators. Furthermore, the drag force increment is approximately 0.15 N when both jets are active. The rise and settling times associated with the onset and termination of the actuation are similar to those of the lift force as discussed in connection to Figure 4.6.

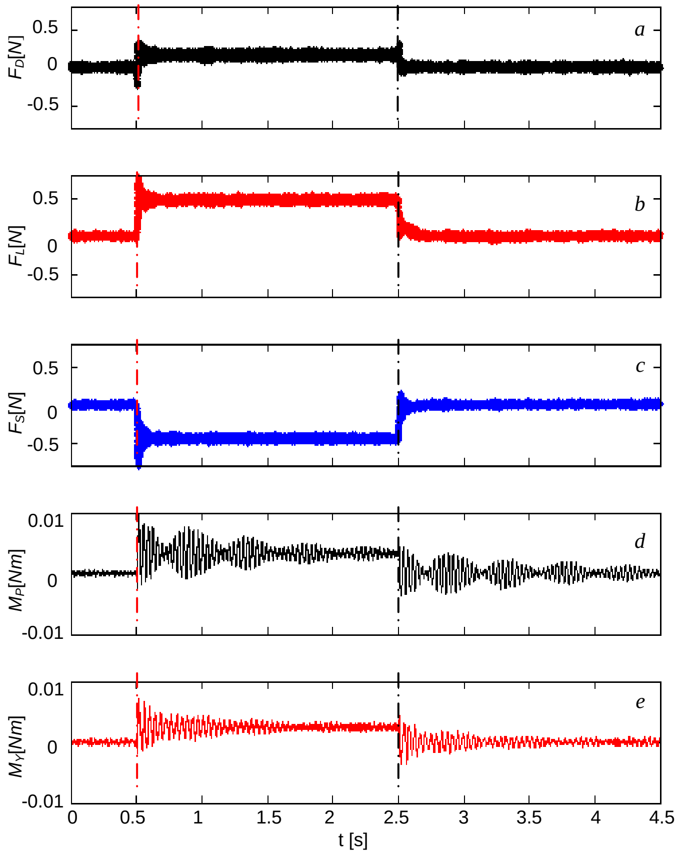

Figure 4.11. *Time traces of the changes in drag (a), lift (b), and side (c) forces, and in the pitch (d) and yaw (e) moments when the flow is continuously actuated by both the top and left jets.*

4.2.1 Transient Response to Onset and Termination of Actuation

In addition to the characterization of changes in aerodynamic forces that can be induced by continuous fluidic actuation, rapid maneuvering of axisymmetric bodies in flight conditions require a minimum transition lag from the time fluidic actuation is activated to the time the change in the force balance is realized. Rinehart et al (2003) investigated such response time for the model attached to the sting and found that the time lag for the full effect of actuation is about 6 ms.

In the present work, phase-locked PIV measurements are used to access the transitory response time to the changes in actuation, where the PIV imaging is triggered by the actuation waveform. Figure 4.12 shows the resulting phase-averaged vorticity and velocity fields for the case of synchronous actuation by both top and bottom jets (C_μ of each jet 1.1×10^{-3}) at $Re_D = 2.13 \times 10^5$. Six instances are selected such that the measurement phases correspond to $t/T = 0$ (onset of actuation), 1, 2, 3, 4, and 5. At the onset of actuation (Figure 4.12*a*), the flow still resembles the baseline (unaltered) flow, similar to Figure 4.8*a*. At the end of one full actuation cycle (Figure 4.12*b*), a single vortical structure is isolated at the tail of the model, and is preceded by large start-up vortex that is shed due to the abrupt discontinuity in the baseline vortex sheet, (this feature of the onset of fluidic actuation is discussed in detail by Vukasinovic and Glezer, 2006). After the second actuation cycle (Figure 4.12*c*), the second vortex is formed at the tail, while the first one is already shed into the shear layer (and preceded by the start-up vortex). The second vortex is not shed into the shear layer, but rather moves inward, as it is seen at t/T=3 (Figure 4.12*d*). As it becomes drawn in the recirculating region, it is also slowed down, and the following, third vortex merges with it, forming the broader vorticity concentration (Figure 4.12*e*). By the time the fourth vortex merges with the previous two (Figure 4.12*f*), the overall flow filed resembles the time averaged flow in Figure 4.12*c*, and the outer flow is drawn inward and reduces the wake width. Therefore, it can be argued that after about five actuation periods the transient onset of the actuation is completed, in excellent agreement with the sting-mounted model of Rinehart et. al. (2003). It is important to recognize that the shed vortices have finite azimuthal extent that scales with the orifice and it is conjectured that their interactions are reminiscent of the evolution of lambda vortices within a plane shear layer.

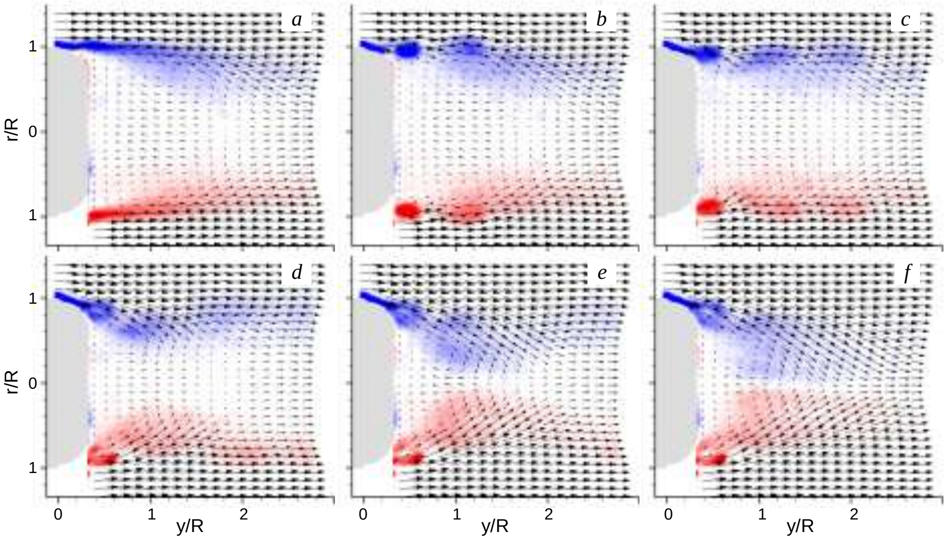

Figure 4.12. *Phase-averaged velocity field and raster plots of the phase-averaged vorticity component ζ^* during the transient onset of actuation at $t/T = 0$ (a), 1 (b), 2 (c), 3 (d), 4 (e), and 5 (f). The flow ($Re_D = 2.13 \times 10^5$) is actuated by both top and bottom jets at $C_\mu = 1.1E\text{-}3$.*

In order to assess the response of the flow to the onset and termination of the actuation, the modulation of the top and bottom actuators is designed to switch abruptly and time-periodically between the top and bottom actuators. This is accomplished by square wave modulation where the period is long enough to allow the transients associated with the bottom actuators to subside. Phase-averaged PIV measurements are obtained phase-locked to the transition from the bottom to the top actuators. Figure 4.13 shows the resulting phase-averaged vorticity and velocity fields for this switch at $t/T = 0$, 1, 2, 3, 4, 5, 6, and 7. Figure 4.13*a* represents the generation of the full downward asymmetric force, as the lower outer flow is vectored upward. At that point in phase the bottom actuation is turned off and the top actuator is activated. Following a full actuation period of the top actuator (Figure 4.13*b*), the first jet vortex is formed, while the bottom flow remains attached to the Coanda surface. The bottom flow remains attached even after the second actuation period and the formation of a second vortex at the top (Figure 4.13*c*), and finally begins to separate from the bottom Coanda surface after the third injected actuation period (Figure 4.13*d*). By $t/T = 4$ (Figure 4.13*e*), the accumulated vorticity near the top edge starts to displace the vectored flow at the bottom up to about $y/R \approx 1.4$, and this trend progresses through the next three actuation periods until at $t/T = 7$, the transitory switch in the vectoring and therefore the lift force is nearly complete. This example indicates that a transient termination of actuation takes longer than the startup, and that relaxation of the forces back to the baseline (unactuated) state is delayed to 7-8 actuation periods, which is attributed to the flow's inherent tendency to remain attached to the Coanda surface.

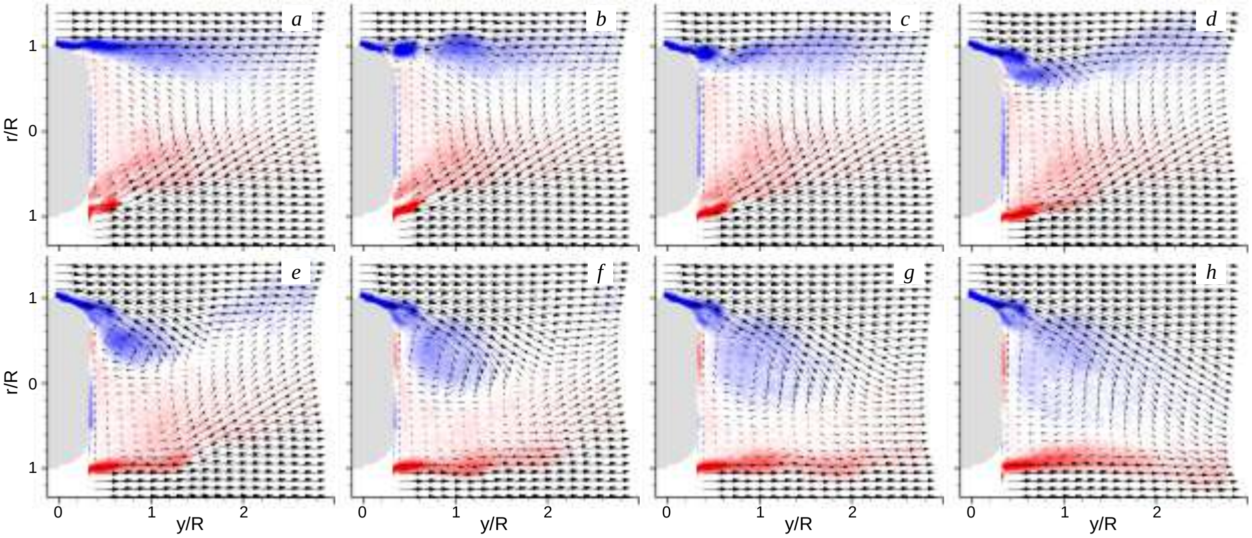

Figure 4.13. *Phase-averaged velocity field and raster plots of the phase-averaged vorticity component ζ^* during the transient switch of actuation at $t/T = 0$ (a), 1 (b), 2 (c), 3 (d), 4 (e), and 5 (f), 6 (g), and 7 (h). The flow ($Re_D = 2.13 \times 10^5$) is actuated by both top and bottom jets at $C_\mu = 1.1E\text{-}3$, such that the top trails the bottom by π in phase.*

4.3 Amplitude Modulation of the Actuation

4.3.1 Enhanced Mixing

In addition to the local flow vectoring by continuous high-frequency actuation, the separated flow behind the axisymmetric model is also controlled by the addition of large-scale vortical motions that are induced by amplitude-modulation of the actuation waveforms. This actuation results in enhancement of the small scale motions of the entrainment by the induced large-scales (e.g., Vukasinovic et. al., 2005).

Two actuation schemes are tested using the top and bottom actuators. In the synchronous mode, the modulation waveforms of the top and bottom actuators are in phase while in the asynchronous mode the modulation waveforms are out of phase so that the actuators are alternately inactive. The modulation frequency is 60Hz, with a duty cycle of 50%.

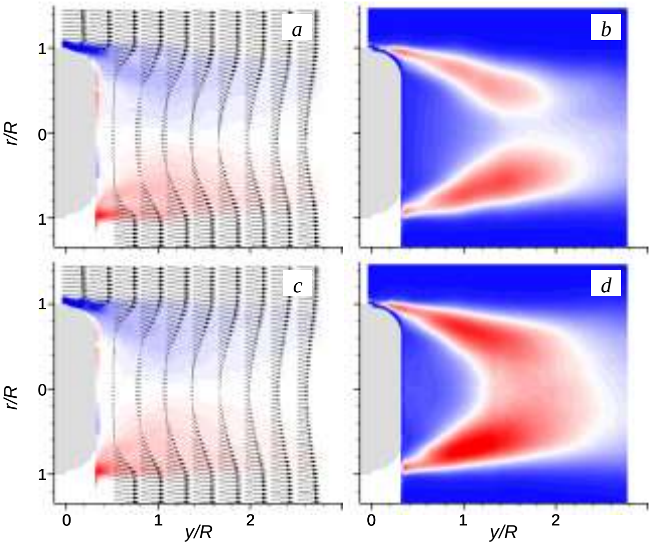

Figure 4.14 *Raster plots of the mean vorticity component* ζ^* *with overlaid equidistant mean velocity profiles (a, c) and turbulent kinetic energy* k^* *(b, d) for the flow (*$Re_D = 2.13 \times 10^5$*) actuated by the top and bottom jets. The control signal is amplitude-modulated at* $St_{AM} = 0.109$ *and modulation of the top and bottom jets are in (a, b) and out (c, d) of phase.* ζ^* *contour levels are the same as in Fig. 4.8.*

The results are shown in Figure 4.14 using raster plots of the mean vorticity with equidistant mean velocity profiles, and 2-D estimate of turbulent kinetic energy (TKE) *k*. Compared to the continuous actuation by top and bottom jets (Figure 4.8*c*), the time-averaged flow fields for synchronous (Figure 4.14*a*) and asynchronous actuation (Figure 4.14*c*), show a similar effect in the wake, in spite of the fact that only half actuator power is used compared to the continuous actuation (at 50% duty cycle). Moreover, the corresponding TKE fields, Figures 4.14*b* and *d*, show a marked increase in the energy levels, compared to the continuous actuation (Figure 4.8*f*). Namely, the peak levels of *k* increase by 50% in the case of synchronous actuation, while in the asynchronous case, it nearly doubles. Such significant increase in turbulent kinetic energy signals the corresponding increase in the mixing and ultimately dissipation in the near wake that is enhanced by large-scale entrainment.

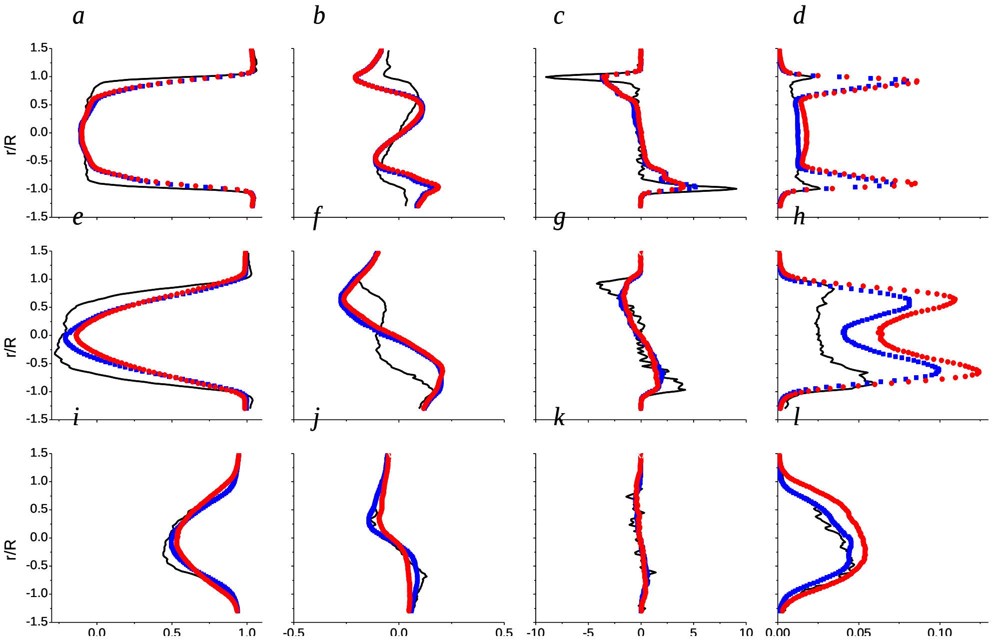

Figure 4.15. *Profiles of the U* (a, e, i), V* (b, f, j), ζ* (c, g, k), and k* (d, h, l) at y/R = 0.5 (a-d), 1.25 (e-h), 2.75 (i-l), for the baseline flow at* $Re_D = 2.13 \times 10^5$ *(—) and the flows actuated by the modulated signal* ($St_{AM} = 0.109$) *in (■) and out of phase (●).*

Similar to the analysis of the representative profiles for continuous actuation, Figure 4.15 shows radial distributions of the mean velocity components, mean vorticity, and turbulent kinetic energy at three downstream locations *y*/*R* = 0.5, 1.25, and 2.75, for synchronous and asynchronous actuation. Along with these two actuation results, the corresponding baseline distributions are also shown as a reference. Most of the details of these distributions are similar to those discussed in connection with Figure 4.8. It is notable that almost all the distributions for synchronous and asynchronous actuation overlap except the distributions of TKE, which are identical at the closest downstream station (Figure 4.15*d*), but farther downstream the levels for asynchronous actuation are higher (Figures 4.15*h* and *l*).

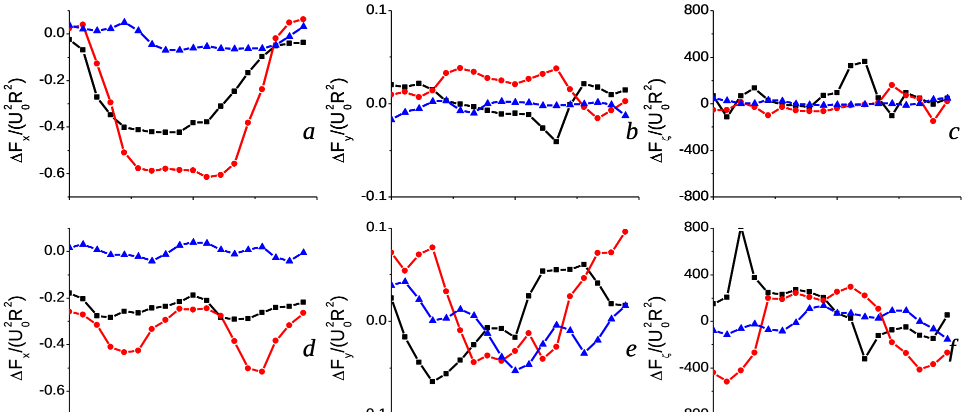

Figure 4.16. *Time-dependent profiles of the change in dimensionless momentum flux in the x- (a, d) and r-direction (b, e), and dimensionless vorticity flux (c, f) relative to the baseline flow, at* $Re_D = 2.13 \times 10^5$ *for the modulated actuation of top and bottom jets (*$St_{AM} = 0.109$*) in (a-c) and out (d-f) of phase at* $y/R = 0.5$ *(■), 1.25 (●) and 2.75 (▲).*

Even though the time-averaged flow fields induced by synchronous and asynchronous actuation modes are almost identical, a closer look at the dynamics of these processes reveals significantly different temporal flow dynamics. To illustrate this difference which is also associated with different dynamic forces, time-resolved momentum and vorticity fluxes are calculated at three streamwise stations y/R = 0.5, 1.25, and 2.75, and the corresponding distributions are plotted in Figure 4.16. The changes in axial momentum flux for the synchronous and asynchronous cases are plotted in Figures 4.16*a* and *d*, respectively. The most significant effect is present at y/R = 1.25 where synchronous actuation increases the reduction in momentum flux until the wake is closed ($t/T \approx 0.3$), and then remains unchanged until the flow starts to relax to the baseline state ($t/T \approx 0.6$). Unlike this time-periodic change at the modulation frequency, the axial momentum flux in the asynchronous case changes time-periodically at twice that frequency. However, the drag reduction is the same regardless of whether the flow is vectored symmetrically at the top or bottom. The radial momentum flux for the synchronous case (Figure 4.16*b*) indicates no change in lift due to the preserved symmetry in the flow at all modulation phases. Although net lift force is zero for the asynchronous case, it actually changes its sign periodically at the modulation frequency (Figure 4.16*e*). Similarly to the discussion of radial momentum flux, there is no change in vorticity flux during synchronous actuation, while asynchronous actuation generates periodic momentary positive and negative fluxes that correspond to the lift forces of alternating signs that add up to zero in the average.

4.3.2 Enhanced Transient Forces

The effects of transitory actuation using amplitude-modulated actuation waveform are investigated by using modulation frequencies that are either close to or much lower than the natural frequencies of the model. Modulation at the model's natural frequency is explored to assess enhancement of the actuation-induced aerodynamic forces and moments. First, the force and moment response to square-wave modulation of the actuation waveform of the top and left actuators (operated simultaneously) is measured over a range of modulation frequencies $10 < f_{\mathrm{M}} < 500$ Hz. The response to the modulated actuation is shown in Figure 4.17 in terms of the variation of the RMS fluctuations of the force/moment magnitude with f_M. The side and lift forces (Figures 4.17*a* and *b*) show considerable increase in of the instantaneous magnitudes at about 100 Hz, with the lift force exhibiting a subharmonic peak. The primary peak of the drag force (Figure 4.17*c*) at 150 Hz is commensurate with the longitudinal resonance frequency (with an additional peak at the subharmonic). The variation of the pitching moment (Figure 4.17*d*) exhibits a peak at 30 Hz, while the absence of a clear peak for the yawing moment which is expected to be at 27 Hz is attributed to the discrete increments (10 Hz) in the modulation frequency.

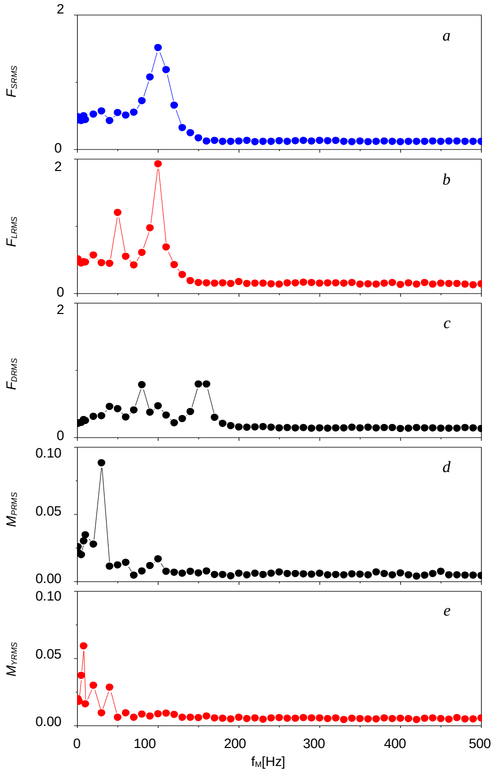

Figure 4.17. *Distributions of the RMS fluctuations of the side (a), lift (b), and drag (c) force, and the pitch (d) and yaw (e) moments with modulation frequency of the continuous actuation by the top and left jets.*

The effects of the modulated actuation are further assessed at $f_M = 100$ Hz, which corresponds to the natural frequency of both lateral and vertical vibrations that are aligned with the active top and left actuators. The transient response of the drag, lift, and side forces of the modulated actuation is shown in Figure 4.18. The actuation starts at $\tau = 0.5$ sec, and as shown in Figure 4.18 the response in the time trace of the drag (Figure 4.18*a*) is different from the responses of the two side forces (Figures 4.18*b* and *c*). Because the modulation frequency does not match the axial natural frequency (along the drag axis), there is no significant increase of the drag force compared to the continuous actuation by the two adjacent actuators (Figure 4.11*a*), but the drag force does oscillate at the modulation frequency. In contrast to this response, there is a nearly threefold increase in the magnitudes of the lift and side forces relative to their levels under the continuous actuation, i.e., transitory magnitudes of 1.5 to 2 N are achieved during the oscillatory force response at the modulation frequency.

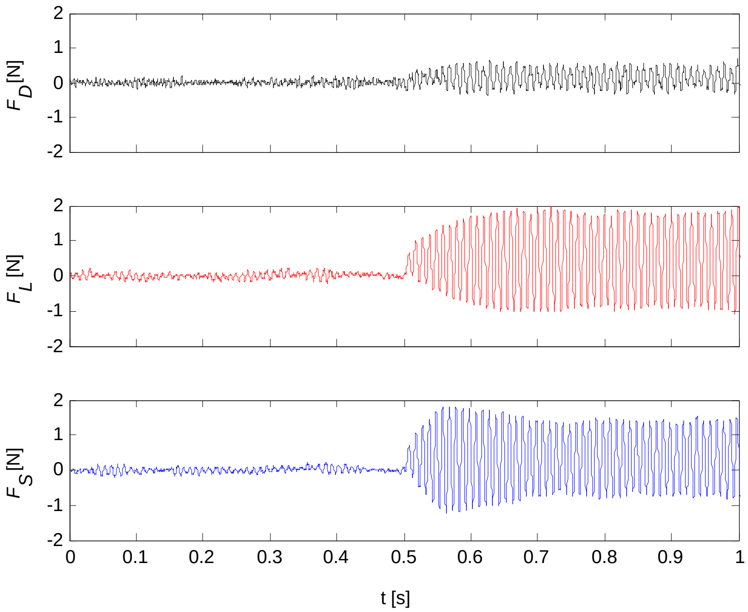

Figure 4.18. *Time traces of the relative measured drag (a), lift (b), and side (c) forces, for the flow actuated by modulation of the top and left jet at 100 Hz.*

The effect of amplitude modulation of the actuation waveform of the top and left actuators, modulated at 100Hz, is shown in Figure 4.19 in terms of the mean velocity and RMS velocity fluctuations at the three streamwise stations within the wake (as in Figure 4.3). Compared to the equivalent continuous actuation (Figures 4.10*a-c*), the qualitative effect of the modulated control input is similar, with several subtle differences. First, since the actuation power is halved with amplitude modulation, the changes in the velocity field of the base wake are less pronounced (Figures 4.19*a-c*). A similar effect is seen in the level of the velocity fluctuation within the wake (Figures 4.19*d*-*f*). As regions of high velocity fluctuations are concentrated within the wake’s shear layer, they migrate the same way as the global wake topology. Thus, domains of high velocity fluctuations are again mostly concentrated on the opposite sides of the wake relative to the active actuators, with one exception that the modulation induces two additional domains of high velocity fluctuations in the vicinity of the actuators, as seen in Figures 4.19*d* and *e*. It is interesting to note that while the modulation at the model’s natural frequency results in high momentary forces and moments, there appears to be little coupling to the wake itself as is evidenced by the relatively small changes in the wake's global topology.

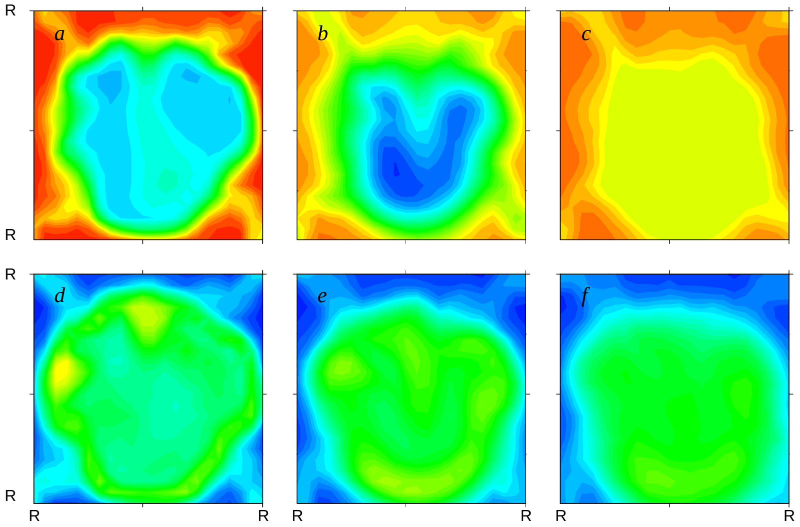

Figure 4.19. *Contour maps of the mean velocity field (a – c) and the RMS velocity fluctuations (d – f) for the flow controlled by the top and left actuators, amplitude-modulated at 100 Hz, at y/R = 0.55 (a, d), 1.5 (b, e), and 2.45 (c, f).*

Spectra of the streamwise velocity (corresponding to the spectra in Figure 4.5) within the wake in the presence of amplitude modulation are shown in Figure 4.20. Comparison between the spectra of continuous actuation in Figure 4.5 shows that the qualitative effect on the wake dynamics is very similar. The main difference is the additional spectral peaks at the modulation frequency and at its higher harmonics as a result of the square wave modulation and flow nonlinearities. The presence of these peaks indicates the formation of vortical structures within the actuated shear layer segment, but with limited spatial extent as can be inferred from the diminished magnitude of the modulation's spectral peaks on the wake's centerline (Figures 4.20*e*-*f*).

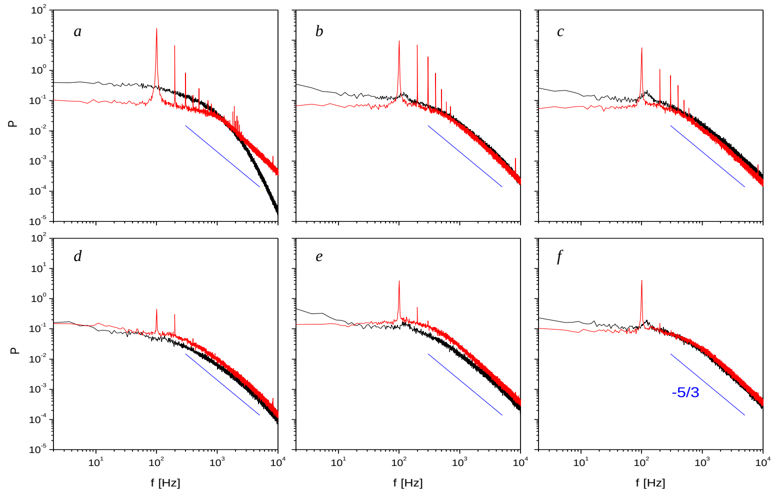

Figure 4.20. *Power spectra of the velocity fluctuations at the upper shear layer (a-c) and the wake core (d-f) for the baseline (▬) and the flow actuated by both continuous top and left jets modulated at 100 Hz (▬) at y/R = 0.55 (a, d), 1.5 (b, e), and 2.45 (c, f).*

4.3.3 Rapid Switching of the Force Direction

Modulation at frequencies that are well below the natural frequencies of the model can yield rapid switching in the force direction between the opposite actuators (as may be needed for trajectory correction), with relatively little coupling to the model's natural frequencies. This is demonstrated by switching between the two opposite actuator pairs (i.e., top-left and bottom-right in Figure 3.1), through phase amplitude modulation of the actuation waveforms. The resulting forces and moments measured for f_M = 2 Hz are shown in Figure 4.21. As the top and left actuators are activated at $\tau = 0.5$

sec, the forces and moments respond in the same manner as for continuous actuation (cf. Figure 4.11). At $\tau = 0.75$ sec, the top-left actuator pair is turned off and the bottom-right pair is simultaneously turned on.

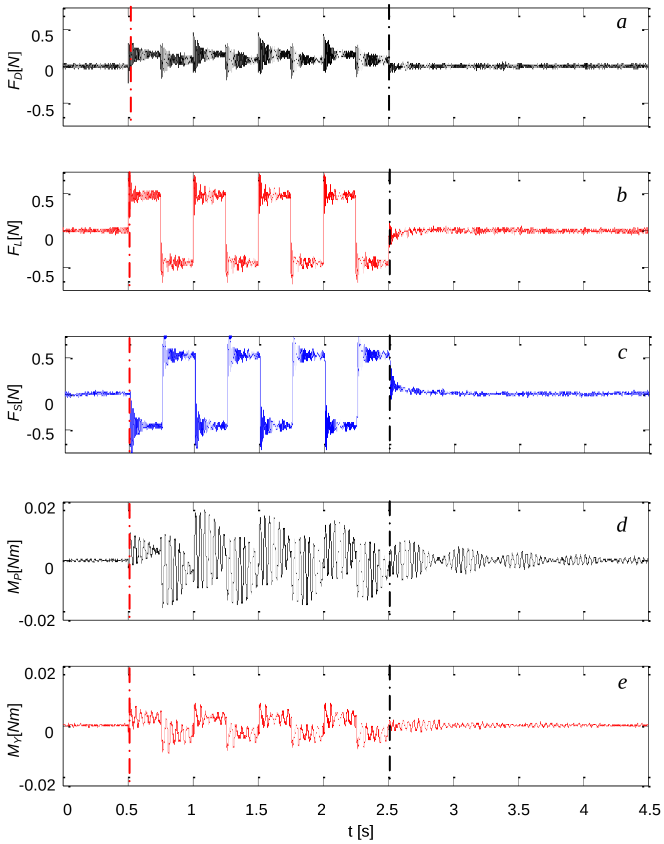

Figure 4.21. *Time traces of the relative measured drag (a), lift (b), and side (c) forces, and the pitch (d) and yaw (e) moments for the flow actuated by modulation of the all jets at 2 Hz, such the top and left jet are run in phase, and the bottom and right jets run out of phase.*

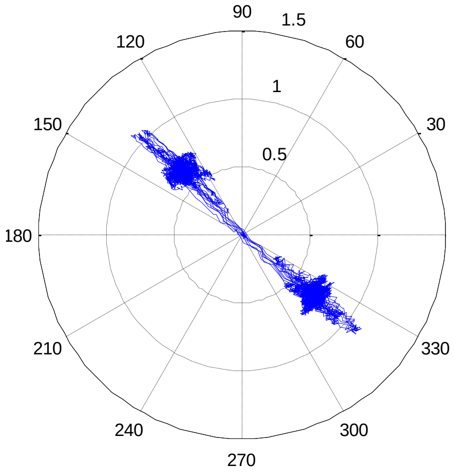

Figure 4.22. *Polar-plot of the resultant fluidic force with its angular position for flow. Actuation case is the same as in Figure 4.21.*

The switching is repeated over four cycles of the modulation waveform exhibiting rapid sign reversal of the forces and moments. The transitory changes in the forces and moments are accompanied by some oscillations at the model's natural frequencies. This is particularly evident in the pitching moment which is strongly affected by the actuation.

The variations in the induced aerodynamic forces shown in Figure 4.21 are also assessed from a polar plot of the angular orientation of the resultant force magnitude during the switch in actuation as depicted in Figure 4.22. These data show that the line of action of the resultant force is at 135° at all times (i.e., along the active actuators' line of symmetry) while the force direction alternates. The force magnitude during the quasi-steady periods is approximately 0.7 N, while during the switching transients, the peak force can reach up to 1.1 N. The direction switching of the induced force can be easily tailored in four quadrants (using the available actuator array) to effect a desired maneuver.

4.4 Spinning Actuation

Time-periodic activation of the actuator array at the tail of the axisymmetric model can be utilized to effect "spinning" time-dependent side forces/moments aimed at continuous trajectory stabilization during flight. The four-actuator array distributed along the model circumference (Figure 3.1) enables different cycles of sequential actuation in either clockwise or counter-clockwise direction.

Five "spinning" actuation cycles are studied, and schematics of the actuation patterns are shown in Figure 4.23. Four repetitions of the actuation pattern are nominally executed during a 2-sec period. Figure 4.23 shows a single actuation pattern that is completed in 0.5 sec. The first actuation pattern is shown in Figure 4.23*a*, where the actuators are addressed sequentially from top to left such that each actuation amplitude is sinusoidally modulated (i.e., begins and terminates at zero actuation). Different sinusoidal modulation patterns of the actuation waveform are shown in Figure 4.23*b*, which enables overlapping transition between neighboring actuators. This overlap is extended in Figure 4.23*c* where two neighboring actuators are simultaneously active during half of each full actuation period, and this pattern is referred to as the double-sinusoidal. Rapid switching is investigated using square-wave modulation as shown in Figure 4.23*d*, with the overlapping pattern in Figure 4.23*e*.

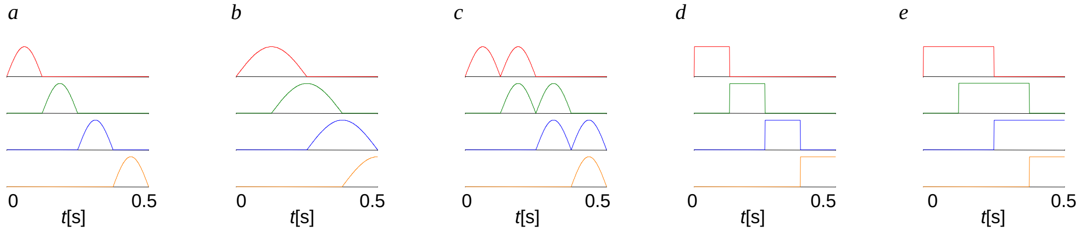

Figure 4.23. Schematics of the spinning actuation cycles depicting sequential activation of the top (▬), right (▬), bottom (▬) and left (▬) jets in: sinusoidal (*a*), overlapping sinusoidal (*b*), double sinusoidal (*c*), square (*d*), and overlapping square patterns (*e*).

The effects of these five spinning actuation patterns are first illustrated by the alterations of the vertical (lift) force increment, as shown in Figure 4.24. During the one full spinning cycle, $0.5 < \tau < 1$ sec, the square-control pattern (Figure 4.23*d*) induces step-like changes in the lift force (Figure 4.24*d*). When the top actuator is first activated ($\tau = 0.5$ sec), a positive upward force is generated. At the point when the actuation is switched between the top and right actuators ($\tau = 0.625$ sec), the vertical force increment vanishes until actuation of the right actuator (horizontal side force) is terminated. Activation of the bottom actuator ($\tau = 0.75$ sec) leads to the generation of a downward vertical force increment until the actuator is turned off and the left actuator becomes active ($\tau = 0.875$ sec) and the vertical (lift) force vanishes again. While the sinusoidal actuation pattern (Figure 4.23*a*) results in a similar force response (Figure 4.24*a*), the transient oscillations at the model's natural frequencies are substantially reduced owing to the gradual switching of the actuation. The variation of the vertical force for the overlapping square modulation (Figure 4.23*e*) is shown in Figure 4.24*e*. The lift force alternates between upward and downward peaks, much like in response to modulation in Figure 4.19*b*. Perhaps the most interesting response of the vertical force is shown for the case of overlapping sinusoidal pattern (Figure 4.23*b*) in Figure 4.24*b*. One spinning cycle generates a quasi-sinusoidal variation of the normal force that is reasonably free of oscillations at the natural frequencies. Finally, the double sinusoidal pattern modifies the previous quasi-sinusoidal force response with the presence of brief intermediate minima (Figure 4.24*c*).

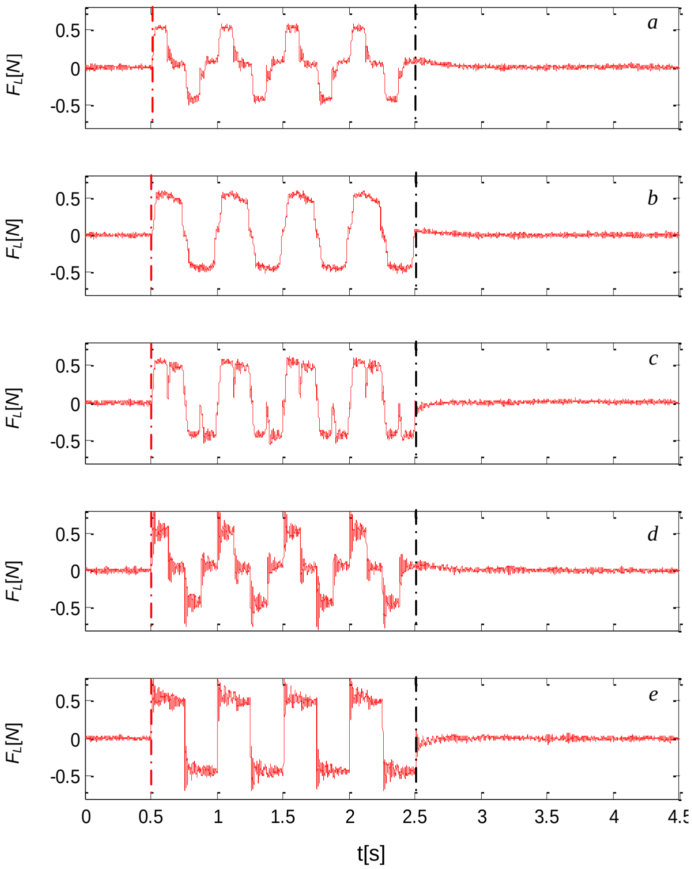

Figure 4.24. *Time traces of the relative measured lift forces for the spinning actuation control by sinusoidal (a), overlapping sinusoidal (b), double sinusoidal (c), square (d), and overlapping square patterns (e).*

The resultant forces that are engendered in response to the five modulation patterns in Figure 4.23 are shown in Figure 4.25 as polar plots of the force magnitude relative to its angular orientation. The square actuation pattern generates a rather complex polar plot (Figure 4.25*d*), where four transient orbits dominate the force trajectory. The transient forces upon actuation reach 0.75N. While the normal force with the sinusoidal actuation is similar to the square actuation, (Figures 4.24*a* and *d*), the polar plot of the resultant force is markedly different (Figure 4.25*a*). The transient oscillations are suppressed, but the resultant force mostly varies between its peaks of about 0.5 N. In the overlapping square pattern, the resultant force trajectory exhibits significant periods during which the resultant force maintains a nearly "square" pattern (Figure 4.25*e*) where at each 45° "corner" in each of the quadrants there are significant transients that are associated with the switching; the transients reach 1N with an average magnitude of 0.75N. These transients are absent in the polar plot of the resultant force during the overlapping sinusoidal modulation (Figure 4.25*b*), where in this case a nearly-constant resultant force, may be achieved by proper adjustments of the time-periodic modulation waveform. Note that only the start-up and termination transients are visible on the polar plot. Finally, actuation with the double sinusoidal pattern (Figure 4.25*c*) leads to a polar plot that somewhat resembles a (45^o) rotated version of the polar plot in Figure 4.25*b*. The corresponding dynamic changes in the pitching moment in response to the spinning actuation (not shown) exhibit a similar pattern. Oscillations at the natural frequencies (30 Hz in pitching) which are triggered by the switching of the modulation are clearly minimized by overlapping sinusoidal actuation (cf. Figure 4.26*d*).

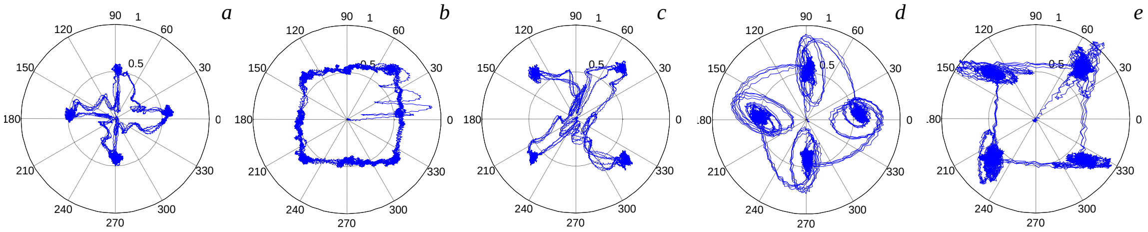

Figure 4.25. *Polar-plots of the resultant fluidic force with its angular position for the spinning actuation control by sinusoidal (a), overlapping sinusoidal (b), double sinusoidal (c), square (d), and overlapping square patterns (e).*

The effectiveness of actuation using the overlapping sinusoidal modulation, which yields a nearly-constant spinning force (Figure 4.26*b*), is investigated in more detail. The response of all the forces and moments to this actuation pattern is shown in Figure 4.26. In addition to the dynamics of the vertical (lift) force and pitching moment that are already discussed above, it is shown that the horizontal side force and yawing moment change in a similar fashion. As expected, the time-dependent side-force is offset in phase from the vertical force by 90°, and the same holds for the yawing moment relative to the pitching moment. It should be noted that the "spinning" force pattern also induces small cyclical variations in drag as shown in the time trace of Figure 4.26*a*.

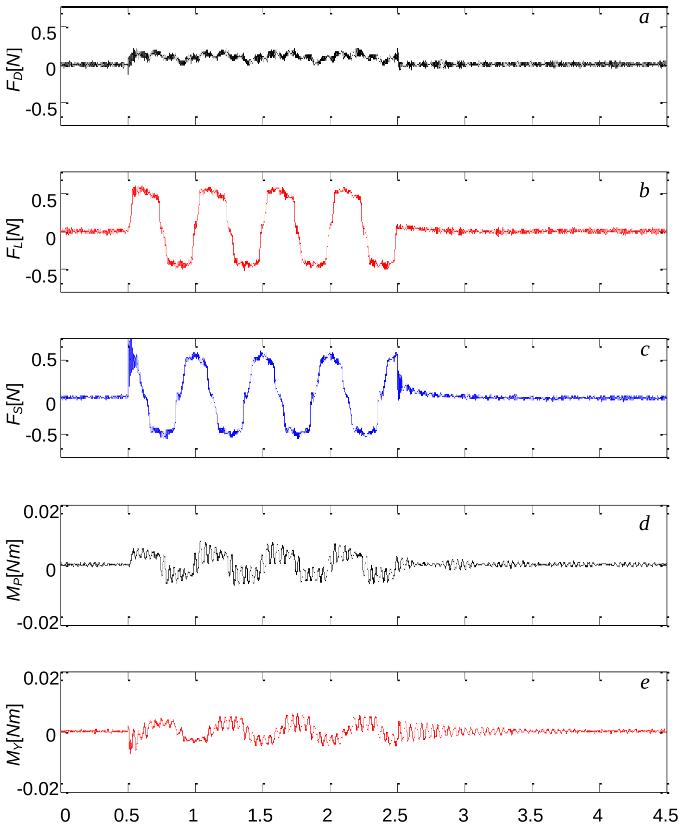

Figure 4.26. *Time traces of the relative measured drag (a), lift (b), and side (c) forces, and the pitch (d) and yaw (e) moments for the flow actuated by the overlapping sinusoidal spinning jets (Figure 4.27b) at 2 Hz spinning cycle .*

The effect of the actuation on the time-averaged streamwise velocity and RMS velocity fluctuations at the three wake cross-sections y/R = 0.55, 1.5, and 2.45 are shown in Figures 4.27*a-c* and 4.27*d-f*, respectively. It is remarkable that compared to the baseline flow, the spinning actuation leads to nearly four-fold symmetry of the time-averaged flow field and velocity fluctuations. The symmetry is clearly associated with the positions of the actuators. Furthermore, the edge of the wake becomes almost circular indicating that the effect of the actuation is somewhat smeared near the edges of the separating share layer segments perhaps owing to phase delays that are associated with the cross stream velocity gradients. The symmetry and uniformity of the actuation is further evidenced by the absence of any deflection of the wake at the farthest measurement station (Figure 4.27*c*). Although a significant increase in the RMS velocity fluctuations is measured in the vicinity of the actuators (Figure 4.27*d*), rapid mixing leads to more uniform distributions farther downstream. While it is clear that the wake responds to the instantaneous changes in the time-periodic spinning actuation, the overall time-averaged symmetry suggests the capability for potential trajectory stabilization.

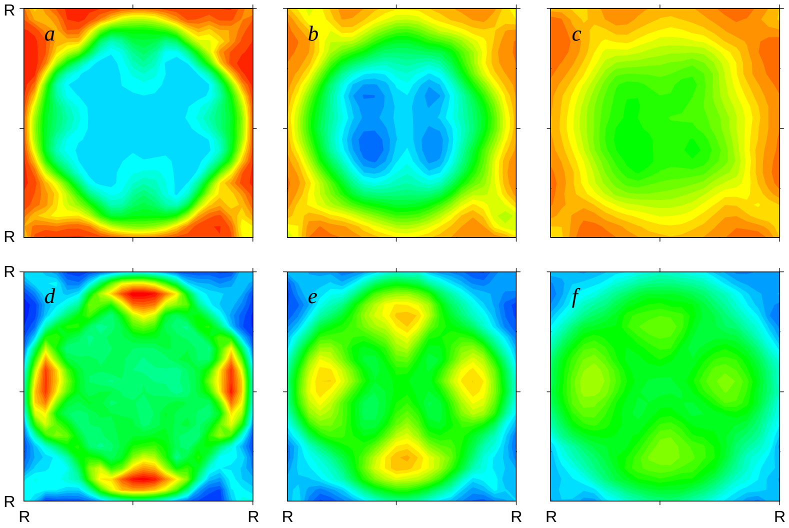

Figure 4.27. *Contour maps of the mean velocity field (a – c) and the RMS velocity fluctuations (d – f) for the flow controlled by the overlapping sinusoidal spinning jets (Figure 4.27b) at 2 Hz spinning cycle at y/R = 0.55 (a, d), 1.5 (b, e), and 2.45 (c, f).*

Finally, the changes in the wake dynamics are characterized using hot-wire spectra within the shear layer and the wake core at the three measurement planes (Figure 4.28). The most prominent feature in these spectra is the increase of energy at the large-scale motions, which is associated with the 2 Hz spinning cycle and with the response of the near wake to the changes in the direction of the induced aerodynamic forces and moments. It is also remarkable that this relatively low-frequency spinning does not appear to induce significant coupling to the natural shedding frequency of the model and in fact, the high-frequency component of the actuation leads to a strong damping of the "background" low frequencies of the near wake at *y/R* = 0.55 indicating that the flow receptivity is primarily confined to the spinning frequency.

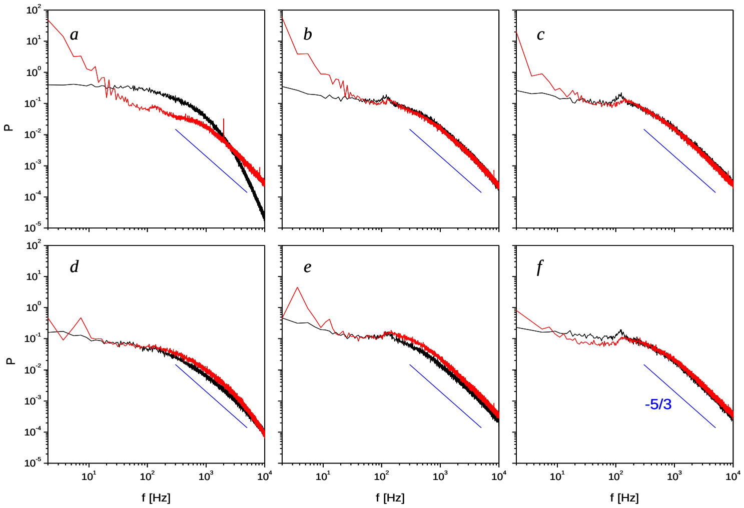

Figure 4.28. *Power spectra of the velocity fluctuations at the upper shear layer (a-c) and the wake core (d-f) for the baseline (▬) and the flow actuated by the overlapping sinusoidal spinning jets (Figure 4.27b) at 2 Hz spinning cycle (▬) at y/R = 0.55 (a, d), 1.5 (b, e), and 2.45 (c, f).*

Chapter 5

Fluidic Control Using a Mid-Body Cavity

The investigation described in this section focuses on the mid-body cavity of an axisymmetric model with the objective to generate steady or transitory asymmetric forces and moments that can be applied for steering. The present approach builds on the control approach that was described in chapter 4, and uses an array of synthetic jet actuators placed azimuthally around the upstream edge of the cavity, in order to turn the outer flow into the cavity.

5.1 Continuous Actuation of the Top Jet

To illustrate the resulting flow field through the cavity upon actuation of a single jet, composite views of the baseline and actuated flows along the cavity (and the jet) plane of symmetry are shown in Figure 5.1 for the top jet actuation at $C_\mu = 1.3\cdot10^{-3}$. The mean velocity and vorticity fields of the baseline flow (Figure 5.1*a*) indicate slight asymmetry between the top and bottom cavity sides. It is also seen that the shear layer that forms off the upstream edge of the cavity impinges the downstream edge, and the outer flow becomes slightly displaced outboard. When the flow is actuated by the top jet (Figure 5.1*b*), there is a significant vectoring of the outer flow into the upper cavity over the Coanda surface, and throughout this section of the cavity. The flow that is deflected into the cavity about the actuator (at the top of the cavity) is leaving at the bottom and penetrates into the outer cross stream. At least within the plane of symmetry, the baselines' recirculating flow is broken and results in a momentum efflux through the cavity's boundary that is shown by a dashed line in Figure 5.1b. Furthermore, the outboard flow from the stagnation point at the downstream cavity wall, gains momentum and penetrates further into the outer flow around the model. The deflected flow leads to the formation of concentration of trapped vorticity of the bottom surface of the model, (only the upstream segment of this vorticity concentration is captured in the measurement plane as shown in Figure 5.1b).

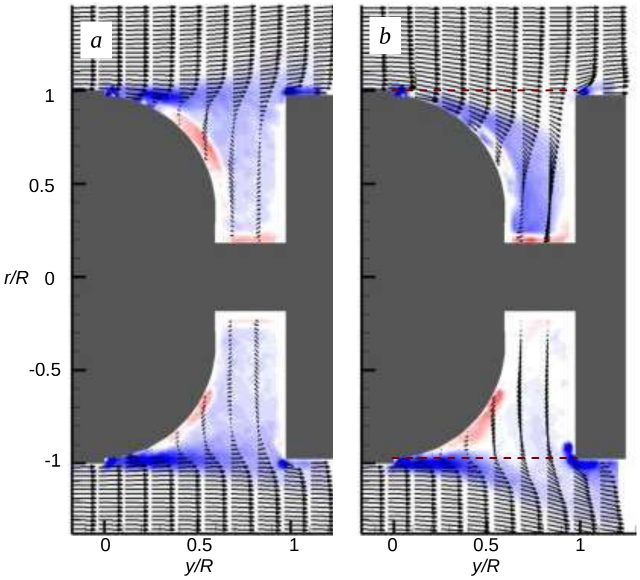

Figure 5.1. *Raster plots of the mean vorticity component* ζ^* *with overlaid equidistant mean velocity profiles measured in the symmetry plane for the flow (*$Re_D = 2.13 \cdot 10^5$*) actuated by the top jet at* $C_\mu = 0.0013$ *(b), and the corresponding baseline flow (a). The cavity boundary is drawn dashed in (b).*

The resulting flow field induces asymmetric forces on the model. First, the change in flow momentum over the Coanda surface generates a force with positive vertical and longitudinal (*z* and *y*) components. A second weaker force may be induced by the relatively weak recirculating bubble off the top of the cavity edge (at the end of the cavity). It should also be noted that these forces also contribute to the streamwise drag force. A force with a cross stream component in the opposite (negative *z*) direction is induced the streamwise turning of the flow out of the cavity (at the bottom). Unlike the flow over the tail section, the utilization of the Coanda-assisted flow vectoring through the mid-body cavity can result in the formation of a force couple and perhaps even a pure moment.

Figure 5.2 shows the streamwise variation of the momentum flux through the upper and lower cavity boundaries in the plane of symmetry in Figure 5.1*b*. The momentum flux through the upper boundary is mostly negative ($0 \leq y/R \leq 0.85$) and reverses direction near the downstream edge ($y/R > 0.85$). The force associated with this flux due to turning in the streamwise direction is probably small. In contrast to the upper boundary, there is virtually no momentum flux through the lower boundary from the upstream edge for $0 < y/R < 0.45$. However, past the cavity midpoint, the momentum efflux steadily increases and reaches a peak that is about three times larger than the largest flux at the upper boundary. It is the streamwise turning of the cross stream momentum flux that results in an induced cross stream force component in an opposite direction to the force component due the momentum flux into the cavity across the top boundary.

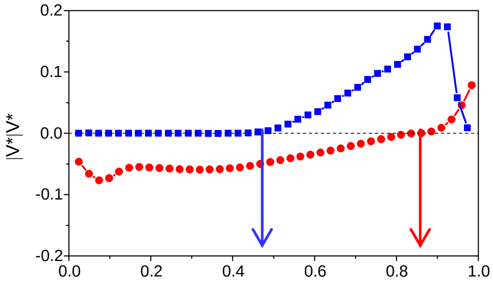

Figure 5.2. *Cross-stream momentum flux components through the upper (●) and lower (■) cavity boundary (as marked in Figure 5.1b) for actuation by the top jet at $C_\mu = 0.0013$. The arrows show the start and end regions of the cavity*

The asymmetric forces and moments that are induced by the actuated cavity are directly measured by the in-line force transducers described in Chapter 3. Figure 5.3

shows the time traces of the phase-averaged force and moment increments that are induced by the operation of the top actuator ($C_\mu = 1.3 \cdot 10^{-3}$, $Re_D = 2.13 \cdot 10^5$). These data show that the segmented vectoring of the flow over the top Coanda surface and induced trapped vorticity over the bottom body surface yield a resultant vertical (lift) force that is nominally about -0.2 N. At the same time, there is also an increase in the pitching moment which is clockwise with respect to the model's cg and therefore corresponds to a nose-up moment. It is noteworthy that along with the change in the lift force, there is also an increase in the drag force of about 0.1N. The slight increase in the side force when the top jet is activated indicates that the resulting cavity dynamics is not symmetric right and left. Perhaps the most interesting result of the aerodynamic force (and moment) control within the mid-body cavity are the two sharp transients of the lift force at the onset ($t = 0.5$ s) and termination of the actuation ($t = 2.5$ s), and the accompanying quasi-steady pitching moment which is 16 times higher in magnitude than that with the aerodynamic control at the tail, (-0.08 N·m, Figure 5.3*d*, compared to 0.005 N·m as by continuous actuation of the top jet in the tail, Figure 4.6*d*). The reason for the large increase in the pitching moment is that the model’s cg sits between the two flow asymmetries, which generate the opposite acting forces. Therefore, the forces are additive in producing the moment. A sharp increase of the (upward) vertical force is measured immediately after the onset of actuation, with the peak magnitude of $F_L = 0.5$ N after 10 ms. Following this peak, the lift force decreases monotonically and changes its sign to $F_L = -0.2$ after about 30 ms from the onset of actuation. Immediately following the termination of actuation, the quasi-steady downward vertical force increases to $F_L = -0.6$ N within about 16 ms before it decreases until the flow relaxes back to its baseline state. The lift force transient response to both the onset and the termination of actuation are shown in Figures 5.3*f* and *g*, respectively. It is noteworthy that the sharp transients associated with the onset and the termination of the jet are not present in the pitching moment, which is attributed to the strong natural oscillations of the model about its lateral axis with the period of 40 ms which presumably dampen force transients with characteristic times of 10 to 16 ms (Section 3.3).

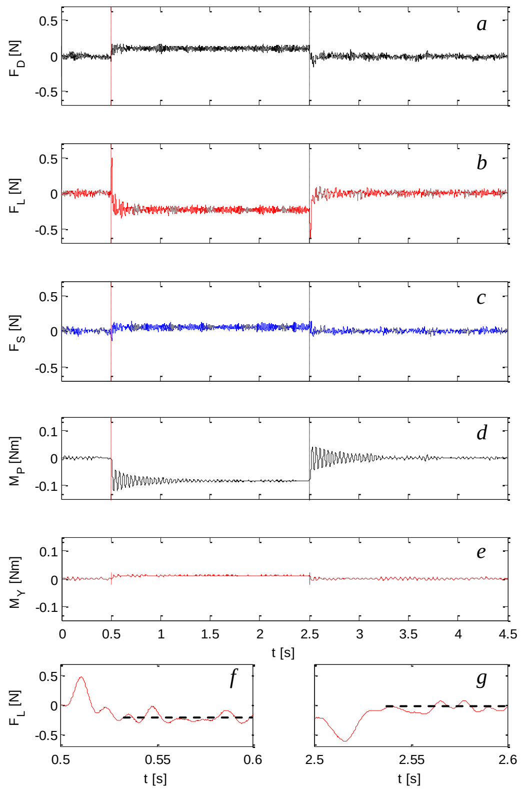

Figure 5.3. *Time traces of the relative measured drag (a), lift (b), and side (c) forces, and the pitch (d) and yaw (e) moments for the flow actuated by the top jet only at* C_μ = *0.0013. Transient lift-force response to onset and termination of the actuation are shown in (f) and (g).*

Figure 5.4 shows the time-averaged distributions of the velocity and vorticity for the baseline and controlled flows at $Re_D = 2.13 \cdot 10^5$. Actuation is applied by the top actuator with increasing jet momentum coefficients, ranging from $C_\mu = 7.1 \cdot 10^{-5}$ (Figure 5.4*b*) to $1.9 \cdot 10^{-3}$ (Figure 5.4*f*). The corresponding baseline flow is shown in Figure 5.4*a*.

The baseline flow field indicates the presence of a typical weak recirculating bubble within the cavity, and a shear layer that forms off the upstream cavity edge and impinges at the downstream edge of the cavity. It is remarkable that even the weakest actuation (Figure 5.4*b*) significantly alters the flow dynamics within the cavity. Upon the actuation, the outer flow is vectored into the cavity, reducing the recirculating domain. Most of the flow near the downstream end-wall of the cavity accelerates downward and the stagnation point at the rear wall of the cavity is displaced downward, and the upward flow along the rear wall slightly penetrates the outer flow at the downstream edge. On the unactuated side of the cavity, the vectored flow penetrates the outer flow at the bottom of the cavity and the shear layer forming off the cavity leading edge is vectored downward and is turned by the outer flow. As the momentum coefficient of the actuated jet is increased, the downstream motion along the rear wall progressively gains momentum; the recirculating bubble moves closer to the upstream Coanda-shaped wall and becomes displaced further downward; and penetration of the stream off the stagnation point becomes stronger with an increase in C_μ.

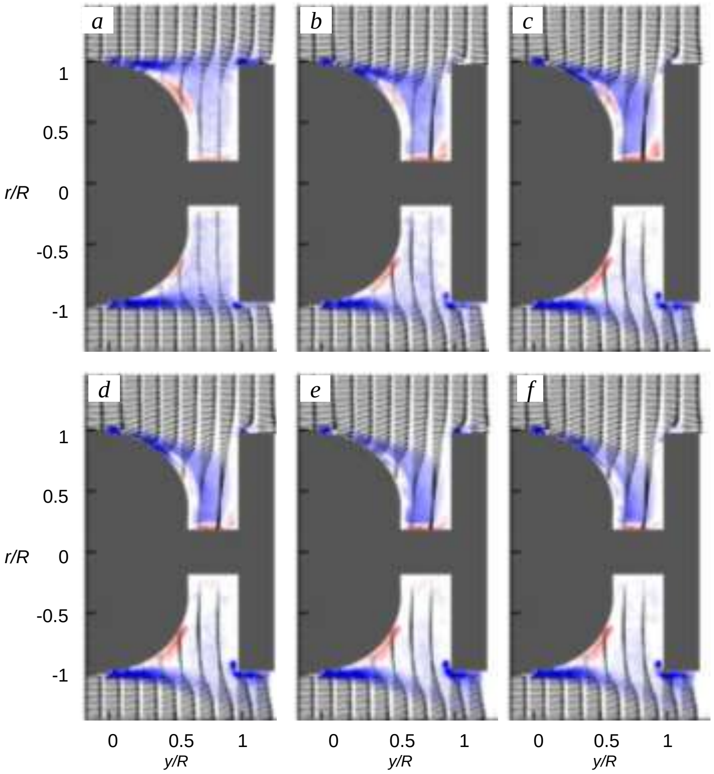

Figure 5.4. *Raster plots of the mean vorticity component ζ^* with overlaid equidistant mean velocity profiles measured at the symmetry plane for the flow ($Re_D = 2.13 \cdot 10^5$) actuated by the bottom jet at C_μ = 0 (a), 7.1E-5 (b), 2.4E-4 (c), 7.7E-4 (d), 1.3E-3 (e), and 1.9E-3 (f).*

Figure 5.5 shows a comparison between the cavity flow at two vertical planes that are equidistant from and on the opposite sides of the symmetry plane. These planes are at $x/R = \pm 0.5$ beyond the azimuthal edges of the active jet so that the jet does not issue directly within the field of view. It is remarkable that the actuation induces notable vectoring of the outer flow even outside the span of the segmented jet orifice and that the effect of the jet spreads azimuthally beyond the jet axis. Figure 5.6 shows three views of the flow dynamics within the central vertical plane (Figures 5.6*a* and *d*), the plane tangential to the connecting shaft that forms the cavity bottom (Figures 5.6*b* and *e*), and the plane that is adjacent to the jet edge (Figures 5.6 *c* and *f*). These data show that the vectoring of the outer flow and downwash through the cavity are strongest along the intermediate plane that is tangential to the shaft indicating the effect of the interference or blockage by the shaft. The images in both planes for the baseline (Figures 5.5*a* and *c*), and controlled flows (Figures 5.5*b* and *d*) imply some asymmetry, which can be partially attributed to slight misalignment of the model. This finding is also in concert with the direct force measurements (Figure 5.3), which shows that the top jet actuation also induces a slight side force.

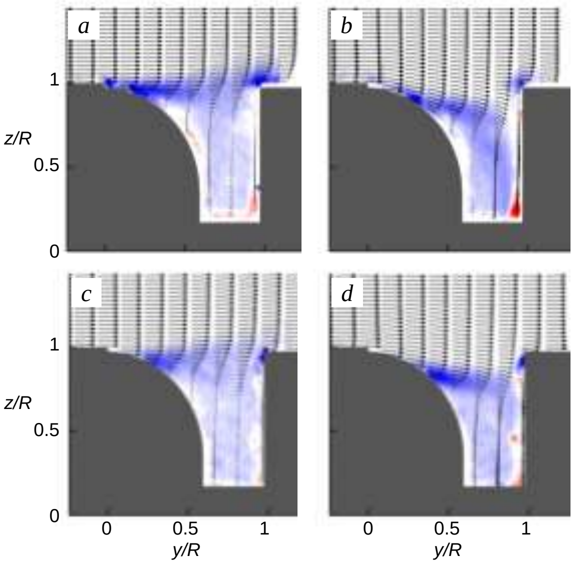

Figure 5.5. *Raster plots of the mean vorticity component* ζ^* *with overlaid equidistant mean velocity profiles measured at* $x/R = 0.5$ *(a, b) and* -0.5 *(c, d) for the flow at* $Re_D = 2.13 \cdot 10^5$ *actuated by the top jet at* $C_\mu = 0$ *(a, c) and 1.3E-3 (b, d).*

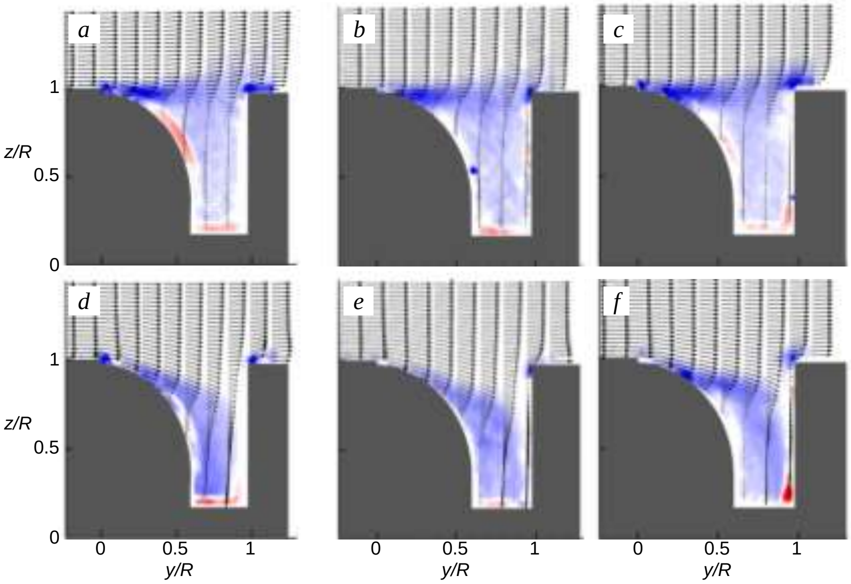

Figure 5.6. *Raster plots of the mean vorticity component* ζ^* *with overlaid equidistant mean velocity profiles for the baseline (*$Re_D = 2.13 \cdot 10^5$*, a – c) and actuated flow by the top jet at* $C_\mu = 1.3E\text{-}3$ *measured at x/R = 0 (a, d), 0.2 (b, e) and 0.36 (c, f).*

As shown in section 4.2, the forces induced by simultaneous operation of multiple actuators around the tail, are additive and there is virtually no interference between adjacent jets. Figure 4.11 shows that the vertical and side forces induced by the jets at the tail are each 0.5 N. It is expected that operation of more than one of the jets within the cavity would induce a joint rather than additive effect, since all the jets issue into a common cavity rather than into the wake. A joint effect of the actuators implies that the jets will partially interfere with each other and each of the normal forces will be less than each jet operating independently. Figure 5.7 shows all the forces and moments induced by simultaneous actuation of the top and right jets along the cavity edge. As a result, the variation of the side force (Figure 5.7*c*) is similar to that of the lift force when only the top jet is active. Similar to the actuation of the top jet, there are transient responses at the onset and termination of the actuation, with the change of the sign and sharp increase in the force magnitude at the onset and termination of the actuation. The quasi-steady force response indicates that the net force is in the direction that is opposite to the force induced by the flow turning over the Coanda surface. Along with the change in the side force, there is also a change in the yaw moment. However, the lift force (Figure 5.7b) has the characteristic response at the onset of actuation, but is minimal for the remainder of the actuation period due to interference of the joint effect between the actuators.

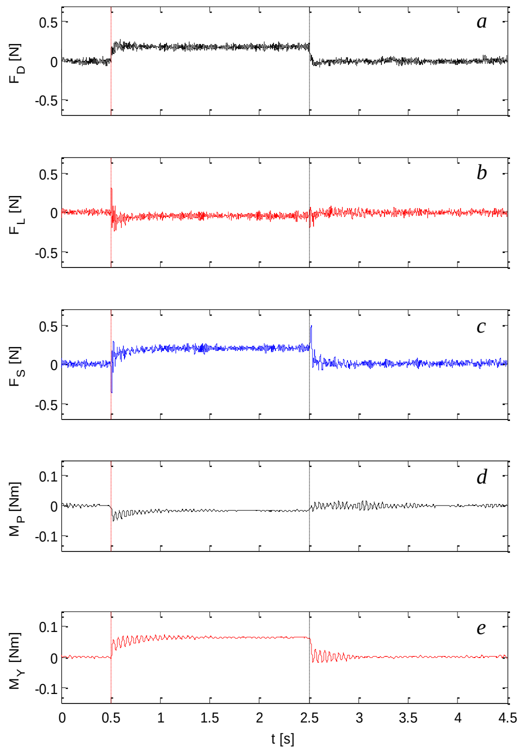

Figure 5.7. *Time traces of the relative measured drag (a), lift (b), and side (c) forces, and the pitch (d) and yaw (e) moments for the flow actuated by both the top and side jet at* $C_\mu = 0.0013$.

5.2 Transient Dynamics

As discussed in connection with Figure 5.3, the coupled transient dynamics of the flow through the cavity yield momentary forces that are substantially higher magnitude and opposite sign than the quasi-steady force. Further insight into the transient dynamics is sought via phase-averaged PIV measurements.

Figure 5.8 shows phase-locked PIV measurements, relative to the onset of actuation by the top jet at *t/T* = 0, 2, 4, 6, 8, 10, 12, 15, 20, 30, 40, and 50 actuation cycles. After two actuation cycles are completed (Figure 5.8*b*), the second CW vortex issued is observed next to the jet orifice, while the first vortex is convected to about *y/R* = 0.3. In addition, also visible is a large start-up vortex centered at *y/R* = 0.9, that is displaced outside of the cavity and into the outer flow, almost reaching the downstream edge of the cavity. After four actuation cycles (Figure 5.8*c*), the three immediate vortical structures remain coherent in the flow field, while the first structure issued is diffused. After six actuation cycles (*t/T* = 6, Figure 5.8*d*), the flow becomes nearly time-invariant. A notable difference relative to the flow field as compared to *t/T*=2, is that the flow immediately downstream from the third issued vortex (*y/R* = 0.3) is now attached to the Coanda surface at *y/R* = 0.4, and is preceded by the second vortex which is displaced downward at about *y/R* = 0.7. It is remarkable that all the other flow fields at later times (Figure 5.8*d*–*l*) are similar which indicates that a time-invariant state of the actuation is reached after four actuation cycles, which is only 2ms. A similar behavior is observed upon transient onset of the top jet at the tail (Section 4.2.1), although it occurs slightly faster at the mid-body cavity. The start up vortex and the first vortex are shed into the wake at the tail, and the second and subsequent vortices move inward (Figure 4.12). The flow on the non-actuated side of the cavity only starts to respond to the actuation after six actuation cycles (Figure 5.8*d*). After eight actuation cycles (Figure 5.8*e*), the flow slowly begins to “open” near the trailing edge of the cavity, and starts to bleed from the bottom of the cavity into the outer flow at about *t/T* = 20 (Figure 5.8*i*). This outflow intensifies with time, and at about *t/T* = 50 (Figure 5.8*l*) becomes time invariant.

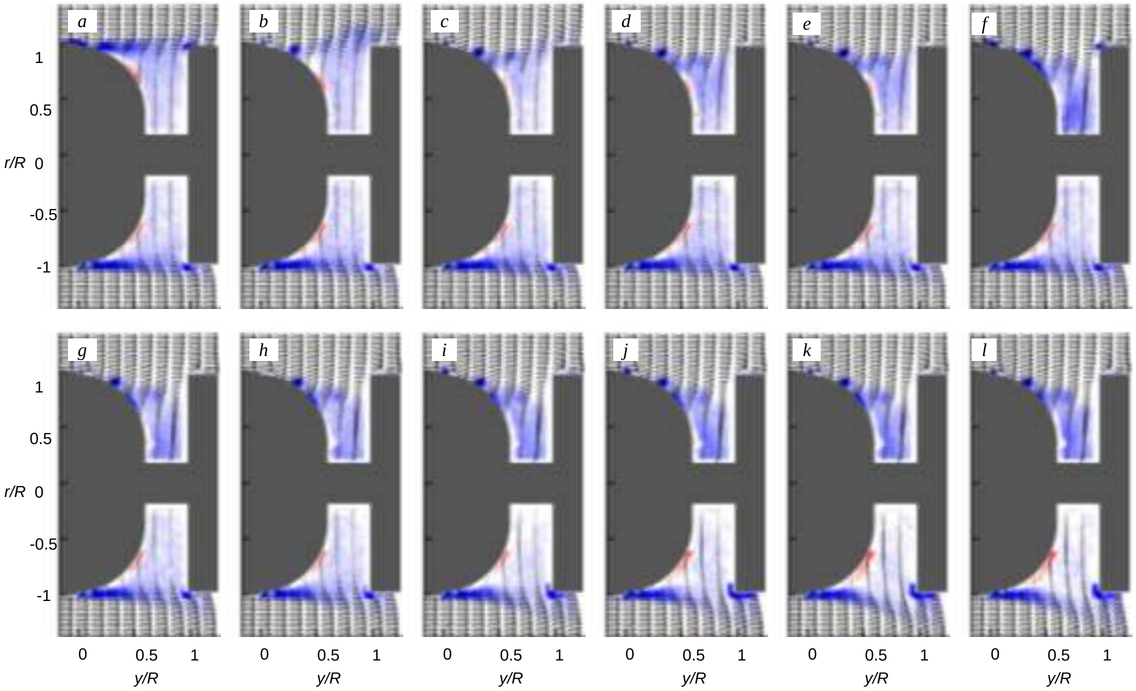

Figure 5.8. *Raster plots of the phase-locked vorticity component* ζ^* *with overlaid equidistant mean velocity profiles* ($Re_D = 2.13 \cdot 10^5$) *for the onset of actuation by the top jet* ($C_\mu = 1.3E\text{-}3$) *at* $t/T = 0$ *(a), 2 (b), 4 (c), 6 (d), 8 (e), 10 (f), 12 (g), 15 (h), 20 (i), 30 (j), and 40 (k) and 50 (l).*

The transient flow response to the termination of actuation is assessed from the corresponding PIV measurements (Figure 5.9). After the last vortices are issued into the flow, the last coherent vortex is seen after *t/T* = 2 (Figure 5.9*b*). After that, the flow remains mostly attached to Coanda surface, but slowly relaxes up to *t/T* = 8 (Figure 5.9*e*) when a reversed flow becomes visible along with CCW vorticity near the surface. This zone of reversed flow continues to creep upstream with time, up until *t/T* = 30 (Figure 5.9*j*), when the flow relaxes back to its baseline state. The flow on the non-actuated side of the cavity remains almost unaffected by the actuation termination up to fifteen actuation periods (Figure 5.9*h*). After this time, it slowly relaxes back to the baseline state, although it does not appear to be fully relaxed even after fifty actuation cycles

(Figure 5.9*l*). At the tail, upon termination of actuation (Section 4.2.1), the flow returns to the baseline state much faster, approximately *t/T* = 8 (Figure 4.13).

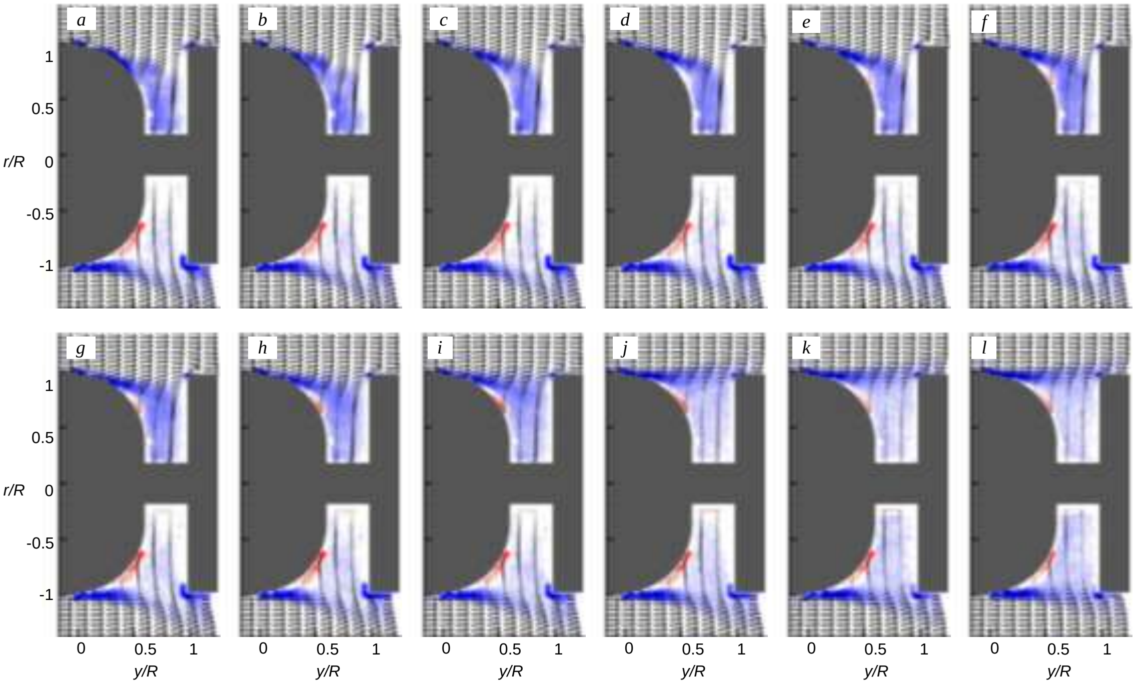

Figure 5.9. *Raster plots of the phase-locked vorticity component* ζ^* *with overlaid equidistant mean velocity profiles* ($Re_D = 2.13 \cdot 10^5$) *for the termination of actuation by the top jet* (C_μ = 1.3E-3) *at t/T = 0 (a), 2 (b), 4 (c), 6 (d), 8 (e), 10 (f), 12 (g), 15 (h), 20 (i), 30 (j), and 40 (k) and 50 (l).*

Similar to the illustration of the mean influx and efflux of the momentum through the cavity's upper and lower boundaries in Figure 5.2, the momentum flux is computed for the phase-averaged transient data in Figures 5.8 and 5.9. The variation of the net momentum flux across each cavity side with phase is shown in Figures 5.10*c–d* along with the corresponding time traces of the transient lift force in 5.10*a–b*. There is a clear relationship between the measured force response and the extracted momentum flux. It is observed that the beginning of a detectable change in lift force upon the actuation onset coincides with the first notable influx of momentum through the upper cavity side (marked as A). As the influx increases with time, and the efflux through the lower boundary is still negligible, the overall lift force increases in magnitude up to the point where there is efflux from the bottom cavity and influx starts to level off (marked as B). From this point onward, the efflux increases faster than the influx, and as a consequence the overall force decreases and eventually changes its sign as the recirculating bubble effect on the bottom surface is established (also seen in Figure 5.3). In addition, upon the termination of actuation, the initial sharp decline of the momentum influx induces an imbalance in the quasi-steady lift force. Consequently, the lift force initially starts to increase in magnitude in the negative direction, as the overall effect becomes biased towards the recirculating bubble (as the influx decreases faster than the efflux, marked as C). After the influx nearly-vanishes (marked as D), the overall force is predominantly downward and from that point it decreases in magnitude with the decrease of efflux, and approaches zero towards the end of the measurement domain.

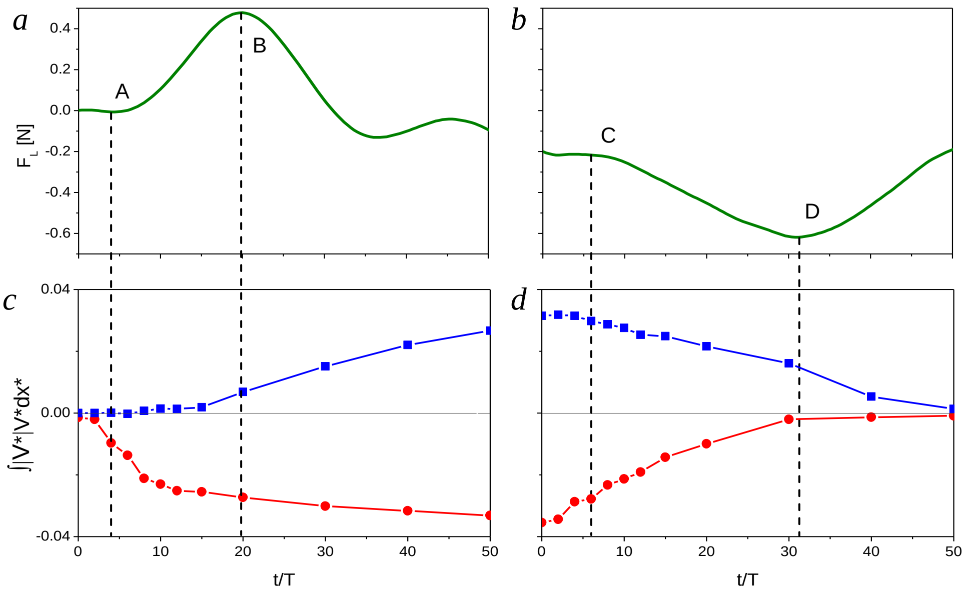

Figure 5.10. *Measured lift force (a, b) and net cross-stream momentum flux components through the upper (●) and lower (■) cavity boundary (c, d) during the transient onset (a, c) and termination (b, d) of actuation by the top jet at* $C_\mu = 0.0013$.

Chapter 6

Conclusions

The aerodynamic forces and moments on a wire-mounted axisymmetric bluff body are altered by induced local attachment of the separated base flow over a Coanda surface using continuous or transitory flow actuation. Control is effected by an array of four synthetic jet actuators that emanate from azimuthally-segmented slots, equally distributed either around the perimeter of a ring-like Coanda surface, either at the tail section or upstream of a mid-body cavity. The actuation results in time-dependent asymmetric forces and moments, that can be used for the in-flight steering and trajectory corrections. Time-periodic variation (or spinning) of the side forces and moments can also be used for stabilization. The effects of the actuation are characterized using direct force and moment measurements by integrated in-line force sensors, and hot-wire anemometry and PIV measurements in the wake.

Full fluidic actuation is achieved at a low actuation momentum coefficient (on the order of 10^{-3} per actuator at $Re_D = 2.13 \cdot 10^5$). The variations of the quasi-steady normal force effected by a single actuator show that for a given free stream speed the induced force first changes rapidly with the jet Reynolds number at low actuation levels (or jet momentum coefficient), but that rate of increase diminishes as the actuation level is increased. In addition, the magnitude of the (dimensional) induced force increases with the free stream speed. Furthermore, it appears that the rate of increase of the normal force coefficient with the jet momentum coefficient saturates and becomes invariant for $C_{\mu sat} > 0.001$. These results indicate that there is a limit on the force coefficient that can be achieved for the fixed model geometry.

Actuation by multiple jets can lead to augmentation and redirection of the induced aerodynamic forces. The largest force is generated when two adjacent jets are activated with monotonic increase in the force coefficient with jet Reynolds number that appears to saturate at $Re_j > 600$. It is shown that continuous actuation can result in steady asymmetric forces of up to 0.7 N (or $C_N = 0.06$). Since the highest level of the induced force is equal to a vector addition of the two orthogonal components that are each induced by a single jet (0.5 N), it may be concluded that there is no interference between the adjacent actuators.

The transients associated with the onset and termination of the actuation have two distinct time scales. The first, fast time scale is the characteristic rise (or fall) time that is typically on the order of $5T_{conv}$ (or $10T_{conv}$) and is associated with the attachment (or detachment) time scale over the tail's Coanda surface. It is conjectured that the longer delay when the actuation is terminated is associated with flows detachment off the Coanda surface. The second, slower time scale is the settling time which is associated with the decay of oscillations that are excited at one of the natural frequency modes of the model which involves the dynamics of the entire model and mounting wires. The settling time following the actuation onset of the lift force is about 48 T_{conv} and is associated with the lower natural oscillation frequency in the vertical direction (about 100 Hz). The termination of the actuation is longer (about 58 T_{conv}) indicating lower damping for model oscillations in the vertical (y-z) plane and is also evident in the oscillations of the pitch increment. Similar patterns are evident in the time series of the side force and yawing moment in the horizontal (x-y) plane. The fast characteristic rise (and fall) times are exploited for rapid switching in the force direction that can be attained within $5\text{-}10T_{conv}$

with significant potential for fast maneuvering applications (the maneuver time clearly depends on the inertia of the model). The present work has also shown that amplitude modulation of the actuation waveform at frequencies that are commensurate with the natural frequencies of the model can lead to strong amplification of the oscillatory aerodynamic forces that can be decoupled from unstable frequencies of the wake. In some instances, the peak force amplitudes can exceed 2.0 N ($C_N = 0.17$). If the waveform modulation is effected at frequencies that are off the fundamental frequencies, out of phase modulation of the actuation waveform of opposite actuators induces asymmetric wake dynamics and aerodynamic forces that alternate with the modulation frequency. During all phases of the modulation, the flow periodically transitions from one limit state in the wake to the other, inducing a significant enhancement of mixing in the near wake.

Several actuation programs that can lead to significant time-periodic (spinning) side forces of controlled magnitude and direction are also explored. Each actuation program is based on sequential azimuthal activation and deactivation of the jet actuators in either CW or CCW directions. In particular, one actuation program is isolated that yields a reasonable-smooth transition between the neighboring actuators and resulted in nearly-sinusoidal, time-varying lift and side forces that are ninety degrees out of phase. The combined effect is nearly-uniform, time-periodic (spinning) side force with highly-damped transient oscillations. This actuation approach may have the potential utility in the stabilization of the model's trajectory in flight.

Unlike control effected at the tail, where the only source of asymmetry was the flow over the Coanda surface, the control of the flow over a mid-body cavity induces two major sources of asymmetry: the directly vectored flow over the Coanda surface at the side of the cavity actuation, and the recirculating bubble formed at the opposite side of the model, downstream from the cavity. These two sources induce a force couple such that the resultant force is the net difference between them. A significant transient variation in the generated force is measured at the onset and termination of actuation. This transient dynamic is attributed to the different transient responses of the cavity flow dynamics on the side that is directly actuated by the jet, and on the opposite non-actuated cavity end. The flow response to actuation on the downstream opposite end takes longer to establish compared to the actuated side. As a consequence, the resulting force is initially generated by the flow response near the actuator, which is progressively offset by the flow evolution on the opposite end. The force effected on the opposite end is larger than the force on the Coanda surface and therefore the net force for the fully-established flow changes in magnitude and its direction before reaching the quasi-steady level. Similarly, when the actuation is terminated, the flow relaxes faster on the controlled side of the cavity leading to a force imbalance where the net force initially increases in magnitude, peaks and then asymptotically vanishes as the cavity flow relaxes to its baseline state. The overall force magnitude between the transient onset and termination spans about 1 N.

REFERENCES

Abramson, P., Rinehart, C. Vukasinovic, B, and Glezer, A., "Fluidic Control of Aerodynamic Forces on a Body of Revolution", *AIAA Paper* 2007-4505, 2007.

Ahuja, K. K. and Burrin, R. H, "Control of flow separation by sound" *AIAA Paper* 84-2298, 1984.

Allen, D., and Smith, B., "Axisymmetric Coanda-Assisted Vectoring", *Experiments in Fluids*, Vol. 46, 2009. pp. 55-64.

Amitay., M, and Glezer, A., "Controlled Transients of Flow Reattachment over Stalled Airfoils", *International Journal of Heat and Fluid Flow*, Vol. 23, 2002, pp.690-699.

Amitay, M., Smith, B., and Glezer, A., "Aerodynamic Flow Control Using Synthetic Jet Technology", *AIAA Paper*, 98-0208, 1998.

Amitay, M., Smith, D., Kibens, V., Parekh, D., and Glezer, A., "Aerodynamic Flow Control over an Unconventional Airfoil Using Synthetic Jet Actuators", *AIAA Journal*, Vol. 39, No. 3, 2001, pp. 361-370.

Bennett, R., and Farmer, M., "Wind-Tunnel Technique for Determining Stability Derivatives from Cable-Mounted Models", *J. Aircraft*, Vol. 15, No. 5, 1978, pp. 304-310.

Cattafesta III, L., Williams, D., Rowley, C., and Alvi, F., "Review of Active Control of Flow-Induced Cavity Resonance", *AIAA Paper*, 2003-3567, 2003.

Chatlynne, E., Rumingny, N., Amitay, M., and Glezer, A., "Virtual Aero-Shaping of a Clark-Y Airfoil Using Synthetic Jet Actuators", *AIAA Paper*, 2001-0732, 2001.

Collins, F., and Zelenevitz J., "Influence of Sound Upon Separated Flow over Wings", *AIAA Journal*, Vol. 13, No. 3, 1975, pp. 408-410.

Colonius, T., "An Overview of Simulation, Modeling, and Active Control of Flow/Acoustic Resonance in Open Cavities", *AIAA Paper*, 2001-0076, 2001.

Corke, T., Tillotson, D., Patel, M., Su, W., and Toldeo, W., "Radius Flow Vectoring for Plasma Drag and Steering Control Using Plasma Actuators", *AIAA Paper* 2008-3769, 2008.

Darabi, A., and Wygnanski, I, "Active Management of Naturally Separated Flow over a Solid Surface. Part 1. The forced Reattachment Process", *Journal of Fluid Mechanics*, Vol. 510, 2004, pp. 105-129.

DeSalvo, M., Amitay, M., and Glezer, A., "Modification of the Aerodynamic Performance of Airfoils at Low Angles of Attack: Trailing Edge Trapped Vortices", *AIAA Paper*, 2002-3165, 2002.

DeSalvo, M., and Glezer, A., "Aerodynamic Control at Low Angles of Attack using Trapped Vorticity Concentrations", *AIAA Paper*, 2006-0100, 2006.

Eaton, J. and Johnston, J., "A Review of Research on Subsonic Turbulent Flow Reattachment", *AIAA Journal*, Vol. 19, No. 9, 1981, pp. 1093-1100.

Englar, R., "Advanced Aerodynamic Devices to Improve the Performance, Economics, and Handling and Safety of Heavy Vehicles", *SAE Technical Paper Series*, 2001-01-2072, 2001.

Englar, R., "Circulation Control Pneumatic Aerodymanics: Blown Force and moment Augmentation and Modification; Past, Present & Future", *AIAA paper*, 2000-2541, 2000.

Freund, J., and Mungal, M., "Drag and Wake Modification of Axisymmetric Bluff Bodies Using Coanda Blowing", *Journal of Aircraft*, Vol. 31, No. 3, 1994, pp.572-578.

Gallas, Q., Holman, R., Nishida, T., Carroll, B., Sheplak, M., Cattafesta, L.," Lumped Element Modeling of Piezoelectric Driven Synthetic Jet Actuators", *AIAA Journal*, Vol. 41, No. 2, 2003, pp. 240-247.

Geropp, D., and Odenthal, H., "Drag Reduction of Motor Vehicles by Active Flow Control Using the Coanda Effect", *Experiments in Fluids*, Vol. 28, 2000, pp.74-85.

Gharib, M., and Roshko, A., "The Effect of Flow Oscillations on Cavity Drag", *Journal of Fluid Mechanics*, Vol. 177, 1987, pp.501-539.

Glezer, A., Amitay, M., and Honohan, A. "Aspects of Low- and High-Frequency Actuation for Aerodynamic Flow Control", *AIAA Journal*, Vol. 43, 2005, pp.1501-1511.

Glezer, A., and Amitay, M., "Synthetic Jets", Annual *Review of Fluid Mechanics*, Vol. 34, 2002, pp. 503-529.

Hammond, D., and Redekopp, L., "Global Dynamics and Aerodynamic Flow Vectoring of Wakes", *Journal of Fluid Mechanics*, Vol. 338, 1997, pp.231-248.

Higuchi, H., Van Langen, P., Sawada, H., and Tinney, C.E., "Axial Flow Over a Blunt Circular Cylinder with and without Shear Layer Reattachment", *Journal of Fluids and Structures*, Vol. 22, 2006, pp. 949-959.

Howard, F., and Goodman W., "Axisymmetric Bluff-Body Drag Reduction Through Geometrical Modification", *Journal of Aircraft*, Vol. 22, No. 6, 1985, pp.516-522.

Hsiao, F. B., Liu, C. F., and Shyu, J. Y., "Control of Wall-separated Flow by Internal Acoustic Excitation", *AIAA J.*, Vol. 28, 1990, pp. 1440-1446.

Huang, L., Maestrello, L., and Bryant, T., "Separation Control Over an Airfoil at High Angles of Attack by Sound Emanating From the Surface", *AIAA paper*, 87-1261, 1987.

Kiya, M., Mochizuki, O., Tamura, H., Nozawa, R., Ishikawa, R., and Kushioka, K., "Turbulence Properties of an Axisymmetric Separation-and-Reattaching Flow", *AIAA Journal*, Vol. 29, No. 6, 1990, pp. 936-941.

Koenig, K., and Roshko, A., "An Experimental Study of Geometrical Effects on the Drag and Flow Field of Two Bluff Bodies Separated by a Gap", *J. Fluid Mechanics*, Vol. 156, 1985, pp.167-204.

Kornilov, V., "Skin-Friction Reduction on Body of Revolution Using Boundary-Layer Alteration Devices", *AIAA Journal*, Vol. 43, No. 10, 2005.

Kurn, A., "Drag Measurments on a Series of Afterbodies at Transonic Speeds Showing the Effects of Sting Interference", *Aeronautical Research Council Current Papers*, C.P. No. 984, 1968.

Lim, D., and Redekopp, L., "Aerodynamic Flow-Vectoring of a Planar Jet in a Co-Flowing Stream", *Journal of Fluid Mechanics*, Vol., 450, 2002, pp. 343-375.

Magill, C., Cataldi, P., and Morency, J., "Demonstration of a Wire Suspension for Dynamic Wind Tunnel Testing", AIAA Paper, 2004-1296, 2004.

Magill, C., and Wehe, S., "Initial Test of a Wire Suspension Mount for Missile Virtual Flight Testing", *AIAA Paper* 2002-0169, 2002.

McMichael, J. M., Lovas, J. A., Plostins, P., Sahu J., Brown, G., and Glezer, A., "Micro adaptive Flow Control Applied to a Spinning Projectile," *AIAA Paper* 2004-2512, 2004.

Mendoza, J., and Ahuja, K., "Cavity Noise Control Through Upstream Mass Injection from a Coanda Surface", *AIAA Paper*, 96-1767, 1996.

Neuberger D. and Wygnanski I., "The Use of a Vibrating Ribbon to Delay Separation on Two Dimensional Airfoils", Proceedings of Air Force Academy Workshop in Unsteady Separated Flow (Colorado Springs, CO), F.J Seiler, ed., Report TR-88-0004, 1987.

Newman, B.G., “The Deflexion of Plane Jets by Adjacent Boundaries- Coanda Effect”, *Boundary Layer and Flow Control 1*, edited by Lachmann, G. V., Permagon, London, 1961, pp. 232-264.

Parsons, J., Goodson, R., and Goldschmied, F., “Shaping of Axisymmetric Bodies for Minimum Drag in Incompressible Flow”, *Journal of Hydronautics*, Vol. 8, No., 3 1974.

Powers, S., “Flight Tests of External Modifications Used to Reduce Blunt Base Drag”, *Journal of Aircraft*, Vol. 28, No. 8, 1991, pp.517-524.

Riesenthal, P., Nagib, H., and Koga, D., “Control of Separated Flows using Forced Unsteadiness”, *AIAA Paper* 85-0556, 1985.

Rinehart, C., McMichael, J. M., and Glezer, A., “Transitory Flow and Force Development on a Body of Revolution using Synthetic Jet Actuation”, *AIAA Paper* 2003-0618, 2003.

Ritchie, S., Lawson, N., and Knowles, K., “Application of Particle Image Velocimetry to Transonic Cavity Flows”, *AIAA Paper*, 2005-1060, 2005.

Roa, S., *Mechanical Vibrations, Second Edition*, New York: Addison-Wesley, 1990.

Rossiter, J., “Wind-Tunnel Experiments on the Flow over Rectangular Cavities at Subsonic and Transonic Speeds”, *Aeronautical Research Council Reports and Memoranda*, No. 3438, 1964.

Sahu, J., and Heavey, K., “Computational Fluid Dynamics Modeling of a 40-mm Grenade With and Without Jet Flow”, *Army Research Laboratory*, ARL-TR-2572, September, 2001.

Sarohia, V., and Massier, P., “Control of Cavity Noise”, *Journal of Aircraft*, Vol. 14, No. 9, 1974, pp. 833-837.

Seifert, A., Bachar, T., Koss, D., Shepshelovich, M. and Wygnanski, I., “Oscillatory blowing: A Tool to Delay Boundary Layer Separation”. *AIAA Journal*, Vol. 31, 1993, pp. 2052-2060.

Sigurdson, L., “The Structure and Control of a Turbulent Reattaching Flow”, *Journal of Fluid Mechanics*, Vol. 298, 1995, pp. 139-165.

Smith, B, and Glezer, A., “Jet Vectoring using Synthetic Jets”, *Journal of Fluid Mechanics*, Vol. 458, 2002, pp. 1-34.

Smith, B., and Glezer, A., “The Formation and Evolution of Synthetic Jets”, *Physics of Fluids*, Vol. 10 No. 9, 1998.

Vukasinovic, B., Lucas, B., and Glezer, A., "Controlled Manipulation of Small- and large- Scales in a Turbulent Shear Layer, Part I: Experimental Studies", *AIAA Paper*, 2005-4753, 2005.

Vukasinovic, B., and Glezer, A., "Transitory fluidic control of turbulent shear flows", *AIAA Paper* 2006-3227, 2006.

Weickgenannt, A., and Monkewitz, P., "Control of Vortex Shedding in an Axisymmetric Bluff Body Wake," *European Journal of Mechanics-B/Fluids,* Vol., 19, 2000.

Wille, R., and Fernholz, H., "Report on the First European Mechanics Colloquium on the Coanda Effect", *Journal of Fluid Mechanics,* Vol. 23, 1965, pp.801-819.

Wu, J.Z., Lu, X.Y., Denny, A. G., Fan, M., and Wu, J.M., "Post Stall Flow Control on an Airfoil by Local Unsteady Forcing," *Journal of Fluid Mechanics,* vol. 371, 21-58, 1998.